NUMERICAL MODELLING AND OBSERVATIONS OF NUCLEAR-EXPLOSION CODA WAVEFIELDS

A Thesis Submitted to the College of
Graduate Studies and Research
in Partial Fulfillment of the
Requirements for the Degree of
MASTER OF SCIENCE
In Geophysics
in the Department of Geological Sciences
University of Saskatchewan
Saskatoon

by

CHAOYING ZHANG

PERMISSION TO USE

In presenting this thesis in partial fulfilment of the requirements for a Master degree from the University of Saskatchewan, I agree that the Libraries of this University may make it freely available for inspection. I further agree that permission for copying of this thesis in any manner, in whole or in part, for scholarly purposes may be granted by the professor or professors who supervised my thesis work or, in their absence, by the Head of the Department or the Dean of the College in which my thesis work was done. It is understood that any copying or publication or use of this thesis or parts thereof for financial gain shall not be allowed without my written permission. It is also understood that due recognition shall be given to me and to the University of Saskatchewan in any scholarly use which may be made of any material in my thesis.

Requests for permission to copy or to make other use of material in this thesis in whole or part should be addressed to:

Head of the Department of Geological Sciences

University of Saskatchewan

Saskatoon, Saskatchewan (S7N 5E2)

Canada

OR

Dean
College of Graduate Studies and Research
University of Saskatchewan
107 Administration Place
Saskatoon, Saskatchewan S7N 5A2 Canada

ABSTRACT

Frequency-dependent earthquake coda attenuation values are often reported; however such measurements usually depend on the types of the attenuation models employed. In this thesis, I use numerical modeling of Peaceful Nuclear Explosion (PNE) codas at far regional to teleseismic distances to compare two of such models, namely the conventional frequency-dependent attenuation with parameters (Q_0, η) defined by $Q_{coda}(f) = Q_0 f^{\eta}$ and frequency-independent effective attenuation (Q_e) with geometrical attenuation (γ). The results favour strongly the (γ, Q_e) model and illustrate the mechanisms leading to apparent $Q_{coda}(f)$ dependencies. Tests for variations of the crustal velocity structures show that the values of γ are stable and related to lithospheric structural types, and the inverted Q_e values can be systematically mapped into the true S-wave attenuation factors within the crust. Modeling also shows that γ could increase in areas where relatively thin attenuating layers are present within the crust; such areas could likely be related to younger and active tectonics. By contrast, when interpreted by using the traditional (Q_0, η) approach, the synthetic coda shows a strong and spurious frequency dependence with $\eta \approx 0.5$, which is also similar to many published observations.

Observed *Lg* codas from two Peaceful Nuclear Explosions located in different areas in Russia show similar values of $\gamma \approx 0.75 \cdot 10^{-2}$ s^{-1}, which are also remarkably close to the independent numerical predictions in this thesis. At the same time, coda Q_e values vary strongly, from 850 in the East European Platform to 2500 within the Siberian Craton. This suggests that parameters γ and Q_e could provide stable and transportable

discriminants for differentiating between the lithospheric tectonic types and ages, and also for seismic coda regionalization in nuclear-test monitoring research.

ACKNOWLEDGMENTS

I am grateful to my supervisor, Dr. Igor Morozov for his patient guidance and generous help throughout my entire Master's study. I greatly benefited from his vast knowledge and keen intuitive understanding of geophysics.

I would like to express my sincere thanks to Dr. Samuel Butler, Dr. Jim Merriam, and Dr. Kevin Ansdell for their time and guidance serving as my committee members. I am also thankful to Mr. Glenn Chubak who was always ready to help me solve various computer problems. Special thanks to Brian Reilkoff and Jennifer Hadley (U of S ITS) for their strong support of Linux computer environment including two clusters.

I would like to acknowledge Dr. Haishan Zheng for helping me to get my study and life started smoothly at University of Saskatchewan. I would also like to acknowledge Dr. Jiakang Li and his wife, Xiyan Bian, for making the beginning of my life in Canada much easier.

I also thank to all other members of Seismology group at the University of Saskatchewan who provided help in various ways over the course of my studies. I would like to extend my thanks to all the students, staff and faculty with whom I have had the pleasure to work alongside over the past few years. I also gratefully acknowledge the funding to the project from the U.S. National Nuclear Security Administration.

Finally, I would like to sincerely thank my husband, Jingyi Chen, who always supports me and encourages me to overcome all kinds of difficulties. My sincere thanks are also given to my cherished son, Kevin Chen, who makes me much happier than I could imagine.

Dedication

To my husband Jingyi Chen and my son Kevin Chen

TABLE OF CONTENTS

page

LIST OF TABLES

page

LIST OF FIGURES

page

LIST OF ACRONYMS

DSS	Deep Seismic Sounding program
GMT	Generic Mapping Tools (software)
IASPEI	International Association of Seismology and Physics of the Earth's Interior
IGeoS	Integrated GeoScience data analysis (software)
IRIS	Incorporated Research Institutions for Seismology
PNE	Peaceful Nuclear Explosion
PVM	Parallel Virtual Machine (parallelization software)
VSP	Vertical Seismic Profiling
WSB	West Siberian Basin

1 INTRODUCTION

1.1 Objectives

Detailed studies of the heterogeneity of the Earth, and especially of its crust, led to several fundamental concepts in modern seismology, and seismic attenuation is one of them. Seismic attenuation, which is usually described by the inverse of the quality factor (Q^{-1}), expresses the reduction of seismic wave energy occurring during wave propagation through the Earth. Unlike geometrical spreading, *Q*-related attenuation is identified by its characteristic increase which is caused by two sources of energy dissipation: intrinsic absorption and scattering. Intrinsic attenuation describes the conversion of elastic wave energy into heat, and it depends on viscous processes involving movements of dislocations through mineral grains (G-Akis Tselentis, 1998) or interactions of the rock matrix with liquid inclusions, such as pore fluids (Gorich and Muller, 1987). By contrast, scattering attenuation represents the deviation of the elastic energy from the propagation direction of the phases of interest, and depends on the spatial distribution of heterogeneities within the medium, and on the magnitudes of velocity and density fluctuations. Both types of attenuation provide critical information about the physical properties and heterogeneity of the Earth's crust and mantle. Understanding of seismic attenuation is also particularly important for understanding the physical laws of elastic energy propagation from earthquake and artificial sources through the Earth's lithosphere.

Earthquake coda waves provide important data suitable for studying attenuation. Codas represent continuous wave trains following all or most of the direct arrivals for

tens to hundreds of seconds. Coda waves are considered as built by the superposition of multiple waves scattered on randomly-distributed heterogeneities and coming to the receiver from all directions. The long durations of the codas, their relatively simple and stable shapes, and averaging over significant volumes of the crust allow reliable measurements of the attenuation parameters, and therefore coda waves are useful for constraining the properties of the lithosphere. However, the attenuation inferred from coda-wave decay rates is still a combination of geometrical spreading, scattering, and intrinsic attenuation, and special care is needed in order to correctly differentiate these factors.

The dependence of Q on the frequency is especially important. The standard mechanical definition for Q implies that it is frequency-independent; however, there also are vast seismological data suggesting strong frequency dependence of $Q(f)$ within the Earth. Numerous studies of body, surface, and coda waves reported frequency-dependent seismic attenuation, while the cause of the frequency dependence of Q still remains poorly understood. Several mechanisms were proposed to explain such frequency dependence and its relation to the procedures of observations. After discarding several possibilities, Aki (1980a) suggested that only the thermoelastic effect and scattering in heterogeneous media were viable (Sneer, 1948; Savage, 1966). These two phenomena require radically different scale-lengths of heterogeneities to explain the observed peak of attenuation around 0.5 Hz: 1 mm and 4 km, respectively. An "absorption band" of strongly increased $Q^{-1}(f)$ at frequencies 0.001 - 1 Hz was recognised within the Earth's mantle (Anderson and Given, 1982). At the same time, some seismologists (such as Morozov, 2008a, 2009), point out that the frequency-dependent $Q(f)$ may still be

apparent and caused by assumptions made during the inversion for Q. In particular, ambiguities of assumed geometrical spreading may affect the measurements of scattering Q, which particularly strongly depends on the frequency. Thus, although numerous recent studies emphasize the importance of seismic scattering in the attenuation, these arguments show the need for additional studies of $Q(f)$ relations and point out the importance of analyzing the lithospheric heterogeneities.

The main objective of this study is to use numerical coda modeling in order to reveal the relation between the coda wave quality factor Q and frequency, and to use coda waves to estimate the scattering and attenuation properties of the Earth's crust. In performing this analysis, I also discuss a new geometrical coda attenuation model (Morozov, 2008a) consisting of a frequency-independent effective attenuation (Q_e) combined with spatially-variable geometrical attenuation (γ). This model is compared to the conventional frequency-dependent $Q(f)$ law $Q_{coda}(f) = Q_0 f^{\eta}$ which has been in broad use since Aki and Chouet (1975). The new model provides a straightforward differentiation between the geometrical and effective attenuation, which incorporates the intrinsic attenuation and small-scale scattering. Unlike the (Q_0, η) description, the inversion for (γ, Q_e) uses only the spectral amplitude data and does not rely on elaborate theoretical models or restrictive (and most often incorrect) theoretical assumptions.

In addition to the modeling study, I compare the results to the observations of the *Lg* wave coda from two Peaceful Nuclear Explosions located in different areas in Russia, and also analyze the correlation of the levels of geometrical attenuation with crustal tectonic types and tectonic ages in many areas around the world. The results suggest that parameters γ and Q_e could provide stable and transportable discriminants for

differentiating between the lithospheric tectonic types and ages, and also for empirical seismic coda regionalization in nuclear test monitoring research.

1.2 Contributions

The problem of frequency-dependent Q is very broad and involves many wave types, frequency bands, and different types of seismic observations. In this thesis, I focused on studying the attenuation properties of the continental crust at short periods (0.5-10 Hz) by using coda waves from nuclear explosions in Russia. The study included both numerical modeling and observations from real data. Specifically, the main contributions of this research are:

1) As an alternative to the $Q_{coda}(f) = Q_0 f^{\eta}$ description, I explored a new attenuation model (γ, Q_e), in which γ stands for geometrical spreading, and Q_e denotes the attenuation quality factor, and applied it to short-period seismic coda. This study represents the first application of this type of model to coda studies.

2) By using a cluster computer system, I performed numerous numerical simulations of the coda in realistic Earth models and tried a broad range of crustal velocity structures and Q values. This study also represents the first attempt for realistic modeling of short-period coda and systematic analysis of the attenuation properties of the model.

3) By using results of numerical simulations, I compared the (Q_0, η) and (γ, Q_e) frequency-dependent Q models and made recommendations about their correctness and suitability. The key contribution here is the demonstration that

apparent, spurious $Q(f)$ dependencies can be observed in models with no frequency-dependent in situ attenuation.

4) Finally, I also measured the coda-wave attenuation in two real Peaceful Nuclear Explosion records in Eurasia, compared the resulting $Q(f)$ and correlated them to the results of modeling. The most important result of this effort is in demonstration that the geometrical contribution to coda $Q(f)$ can be predicted by independent waveform simulations.

1.3 Russian Deep Seismic Sounding Datasets

In order to compare the results of numerical modeling to real data, I analyzed the Peaceful Nuclear Explosion (PNE) data sets acquired by the Russian Deep Seismic Sounding (DSS) program (Figures 1-1 and 1-2). These data covered a large portion of the East European platform and Siberia, with a broad variety of different geological settings.

The Peaceful Nuclear Explosion (PNE) seismic datasets used in this study were acquired by the Deep Seismic Sounding (DSS) program in the former Soviet Union in 1977 – 84. By contrast to the paucity of natural seismicity in Northern Eurasia, DSS data sets provide unusually dense and uniform coverage of this vast area, with hundreds of chemical explosions and dozens of PNEs (Figure 1-1). The DSS program consisted of about 40 PNEs and over 600 chemical explosions which were conducted across the territory of the former Soviet Union in a wide variety of geologic emplacement media (e.g., salt, clay, sandstone, granite, limestone) and are representative of broad ranges in explosion yields and source depth of burial (Sultanov et al., 1999).

The concept of utilizing the weapons of war to serve the peaceful pursuits of mankind is as old as civilization itself. With the ideas on how the explosive force of nuclear devices could be used for scientific purposes or to transform the landscape and alter the character of geological formations deep under the Earth, the former Soviet Union started the process of applying this powerful new sources of energy to the peaceful uses in 1960's.

Starting in 1965, the program "Nuclear Explosions for the National Economy" began field experiments looking at the possibility of using nuclear explosions to increase oil production as well as at planning experiments in salt to produce cavities. In the middle of 1966, a crisis in the gas industry suddenly offered an opportunity for a new application

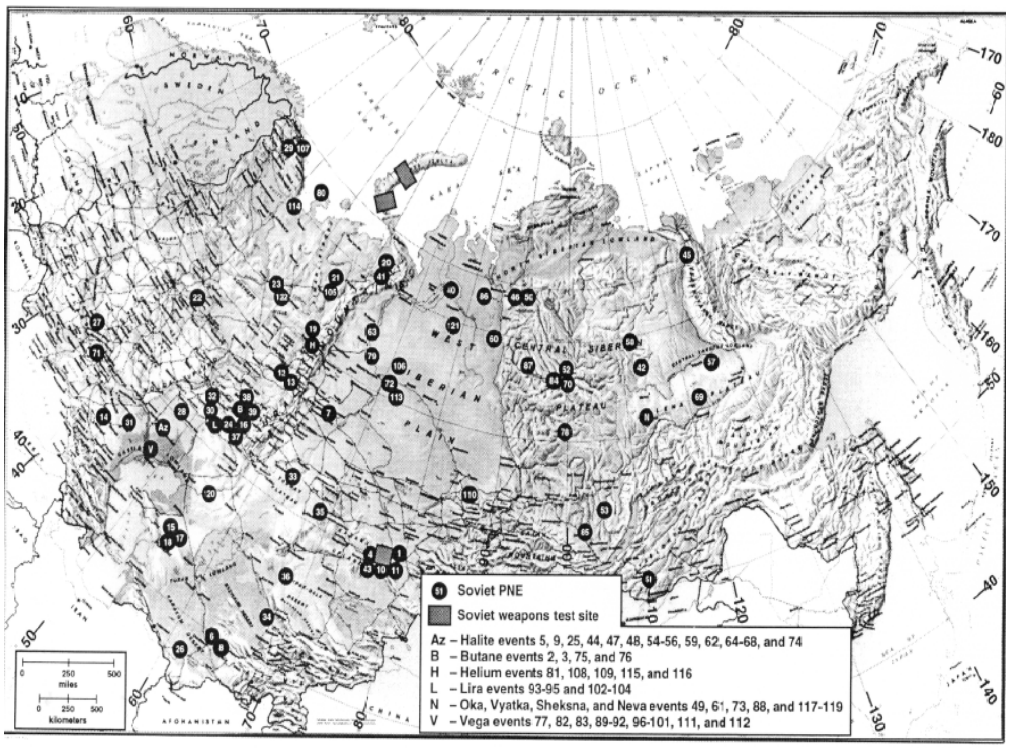

Figure 1-1. Map of the former Soviet Union showing geographic locations of 122 PNE sites. Sites of multiple explosions are indicated by a letter as described in the legend (Nordyke, 2000).

for the PNEs, the extinguishing of runaway gas wells. A few articles appeared in the Russian press in the early seventies describing the general objectives of the Soviet PNE Program.

From 1965 to about 1988, the PNE program carried out 122 explosions involving approximately 128 explosives to study some 13 potential uses (Figure 1-1). In particular, the DSS program produced an enormous volume of seismic data that still are being analyzed to better understand the deep geologic structure of the vast reaches of the Russian subcontinent (Figure 1-2). Although it may potentially assist in the discovery of a few new major hydrocarbon or mineral resources in the future, its main value will

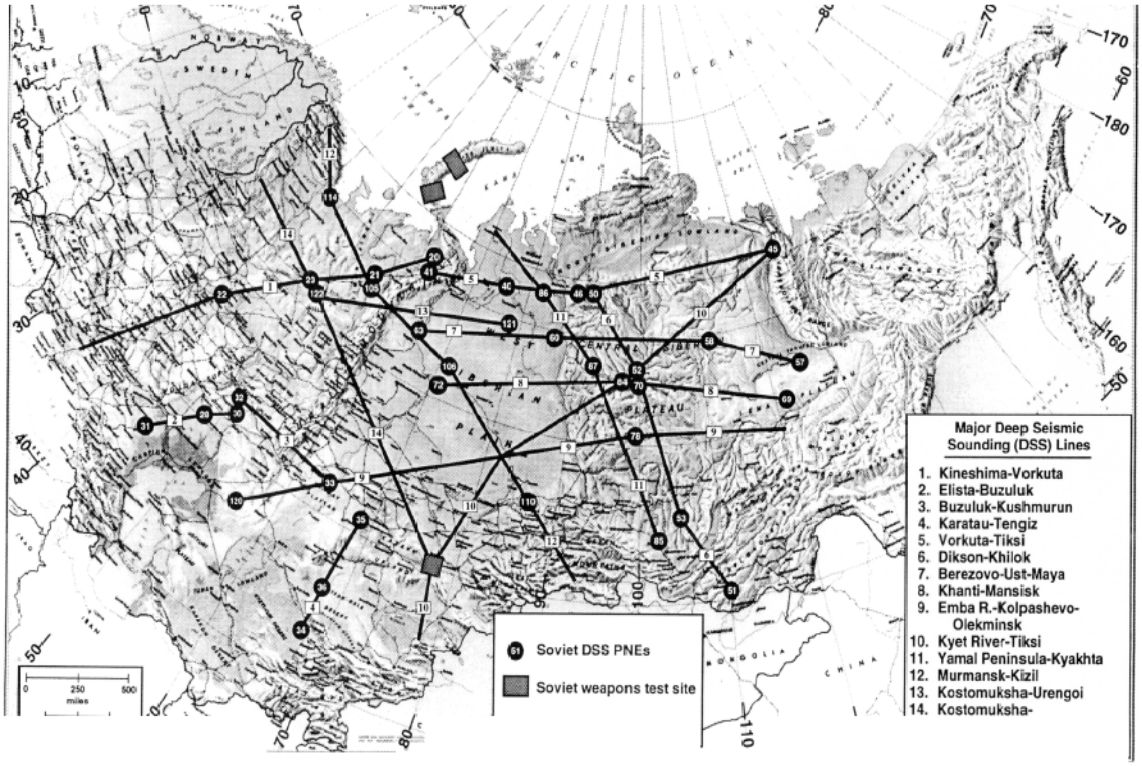

Figure 1-2. Map of the Former Soviet Union showing the location of West Siberia basin, the Deep Seismic Sounding (DSS) explosions and major DSS lines (Nordyke, 2000).

likely be in the geotectonic area.

For the present research, these regional seismic data provide an unparalleled data set on which to perform amplitude and coda measurements. Source-receiver offsets up to 3000 km, nominal receiver spacing of 10 – 15 km, three-component recordings, and presence of both crustal and mantle seismic phases in the records make the dataset unique source of regional seismic information that is still not available elsewhere. Figure 1-3

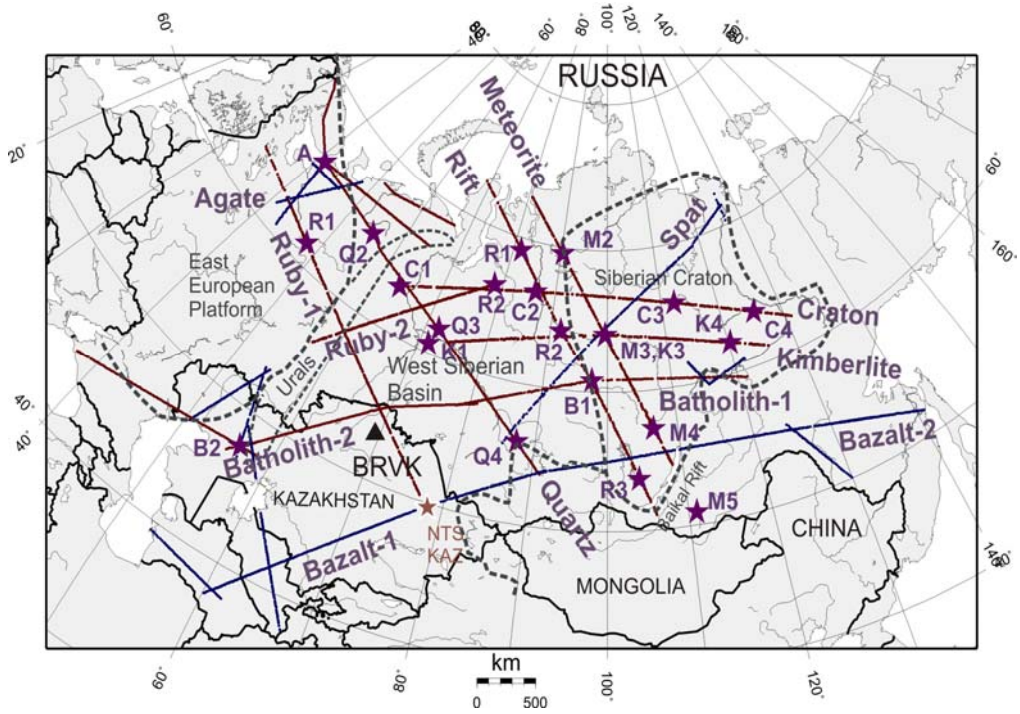

Figure 1-3. DSS PNE projects available at the University of Saskatchewan. Projects are labelled in blue, and labelled purple stars show the PNEs. The data set also includes two Semipalatinsk nuclear test site explosions (red). Parameters of the PNEs were reported by Sultanov et al. (1999). Major tectonic units are indicated. Small brown circles (appearing as lines at station spacing of 10-15 km) are PNE recording stations, and blue circles are chemical-explosion recording stations. Each profile also contains from 30 to 150 chemical explosions. Borovoye International Monitoring System station is also indicated (BRVK) (Morozov, 2006).

shows a map of the DSS profiles available at the University of Saskatchewan and contributed to IRIS (Incorporated Research Institutions in Seismology, a U.S. university consortium) as a part of our research.

1.4 Tectonic and Geologic Setting

This study focuses on very general geophysical properties of the continental crust of northern Eurasia sampled by several DSS PNE profiles. Therefore, the geological description below only outlines the main structures of this vast area. The summary below is based on Zonenshain et al. (1990) and Peterson and Clarke (1991).

The PNE data profiles used in this study are Quartz and Kimberlite (Figure 1-3), which are almost orthogonal to each other and extend across a wide variety of continental structures of Northern Eurasia, from the East European platform, to the West Siberian Basin, and to the Siberian Craton (Figure 1-3). The deep erosion of the underlying Precambrian and Paleozoic basement built the large sedimentary basins of northern Eurasia, followed by subsidence due to the extension of the crust within aulacogens or rifts (Zonenshain et al., 1990; Morozova et al., 1999). From NW to SE, the tectonic structures crossed by the two profiles are as follows (Figure 1-3) (Zonenshain et al., 1990; Morozova et al., 1999).

The **East European platform**, including the Baltic Shield, consolidated at the end of the middle Proterozoic after accretion of smaller continental blocks that joined to form a stable craton. The craton remained virtually intact since the last granitic intrusions

at 1.5 billion years. The Precambrian Baltic Shield is the oldest and most stable part of the East European platform.

The **West Siberian Basin** (WSB) is a giant sedimentary basin with an area exceeding $3.5 \cdot 10^6$ km^2. Structurally, it is a platformal basin, the largest in the world (Peterson et al., 1991). It separates the East European platform and Siberian Craton. The basement of this platform was formed by Paleozoic fold structures and older Precambrian blocks. It is a heterogeneous and multi-aged mosaic containing five types of tectonic units: (1) convergent systems, i.e. extinct island arcs and marginal seas or continental margin arcs; (2) microcontinents; (3) relict ocean basins; (4) rifts; (5) failed oceans. The Basin is bounded by fold belts of different ages: the Late Paleozoic Urals in the west, Early and Late Paleozoic Kazakh Fold Belt in the south, Early Paleozoic Altai and Sajan Folded regions in the southeast, and Late Paleozoic to Early Mesozoic Taymyr in the northeast. The West Siberian Basin, together with fold systems surrounding it, is a northern branch of the Precambrian-Paleozoic Uralian-Mongolian fold belt. Geophysical and geological surveys revealed that the crustal thickness of West Siberian platform ranges from 45 km near the margins of the platform to 29-35 km in the central and north parts (Peterson and Clarke, 1991).

The **Siberian Craton** was assembled between 2.1 and 1.8 billion years (Age) by the collision of several Archaic and early Paleoproterozoic blocks (Rosen et al., 1994; Rosen, 2003), and remained stable since the Permian, The Palaeozoic surface of the West Siberian Basin has subsided. The Siberian Craton has nearly uniform crustal thickness of 40–43 km (Pavlenkova et.al., 2002). Not only has this resulted in deep burial of the

basaltic sequences, but also it has helped create some of the world's largest oil and gas fields (Peterson and Clarke, 1991).

Deep, north-south trending rifts occur within the WSB. These are called the Urengoy (central WSB) and Yenesei (eastern WSB) rifts. Now buried beneath several kilometres of sedimentary rocks, these structures contain thick sequences of Permo-Triassic basalt (see review by Saunders et al., 2005). The relative timing between rifting and volcanism remains unconstrained.

1.5 Computing resources

Modeling and data analysis in this study were mostly performed by using the IGeoS package (Morozov, 2008b), and GMT programs (Wessel and Smith, 1995) were used for making PostScript plots. Below, I give brief summaries of these packages.

IGeoS package. IGeoS– Integrated GeoScience data analysis is a versatile, highly integrated software package used for many seismic processing tasks in a wide range of geophysical data analysis. The modeling and data analysis involved in this project were performed using this package. IGeoS is being continuously developed since the mid-1990's by Prof. Igor Morozov as a framework for integration of geophysical software. It is able to manage and process several types of geophysical data, including: 1) reflection and refraction seismic records in complex 2-D and 3-D survey geometries, 2) multicomponent seismic datasets, local to ultra-long range earthquake and nuclear explosion seismic records; 3) real-time (Internet seismic network) data management, 4) Ground Penetrating Radar records; 5) 1-, 2-, and 3-D seismic waveform simulations, 6) travel-time curves, surfaces, and tables, 7) well logs, 8) 2D and 3D potential-field

datasets, and also 9) various types of velocity and density models, and IGeoS can also be viewed as a framework for integration, development, and maintenance of geophysical software (Chubak and Morozov, 2006).

GMT programs. The Generic Mapping Tools (GMT) were used for making PostScript plots in this research. GMT is an open-source collection of ~60 UNIX tools for manipulating geographic and Cartesian data sets and producing Encapsulated PostScript File (EPS) illustrations. This package was developed by Paul Wessel and Walter H. F. Smith (University of Hawaii), supported by the U.S. National Science Foundation, and is broadly used in academic research around the world.

The GMT package has powerful and elaborate command-line graphic capabilities, and most importantly for this study, it was interfaced with IGeoS.

1.6 Structure of this thesis

In the present **Chapter 1**, the objectives, the data, geological setting, and the resources involved in this research are briefly introduced.

In **Chapter 2**, I first review the development of coda wave analysis and present a simple theoretical treatment of scattering and attenuation. After this, I discuss the existing arguments for frequency-dependent and independent coda Q and also describe the new parameterization of attenuation (γ, Q_e), which may be used instead of the conventional parameters Q_0 and η. Following this, I describe the key concepts of coda Q on which this study is based.

In **Chapters 3 and 4**, I analyze and compare the (Q_0, η) and (γ, Q_e) parameterizations of coda attenuation by using numerical examples. Chapter 3 presents

the modeling part of this research. I start by creating synthetic PNE Green's Functions, a numerical coda model, and synthetic coda waveforms, followed by generating four finite-difference models of PNE coda wavefields in realistic crustal and upper mantle velocity models. These models are then tested for variations of crustal velocities and *Q*. In Charter 3, I analyze the modeling results and interpret the dependence of modelled coda *Q* on the frequency. In Chapter 4, I present observations of real nuclear-explosion coda wavefields, and compare them to the numerical modeling results. The results of these Chapters were included in Morozov et al. (2008).

In **Chapter 5**, based on a worldwide data compilation, I discuss the relation of coda attenuation properties to the tectonic types of the Earth's crust. I also describe a procedure for inverting the coda *Q* data for the *in situ* scattering properties of the crust. Chapter 5 also gives the final conclusions from this work, an evaluation of the significance of the results, and suggestions for further studies.

Finally, in **Appendix A**, I give some technical aspects of implementing the modeling and processing using the IGeoS processing system. In particular, this Appendix presents results of modeling speed-up tests conducted using parallel modeling software on our cluster computer system.

2 OVERVIEW OF CODA WAVEFIELD

2.1 The development of coda wavefield analysis method

Originally the term ‘coda’ referred to the oscillations of the ground continuing long after the latest arrival time of any theoretical surface wave (Ewing et al., 1957). Later, in order to describe the tail part of the seismograms of local earthquakes, a more general meaning was assigned to this term by seismologists who studied seismic waves from local earthquakes (Aki, 1969; Takano, 1971). This seismogram tail contains the energy recorded after the passage of the primary waves, and the word ‘coda’ was used to refer to all gradually decaying wave trains following the primary waves. If only body

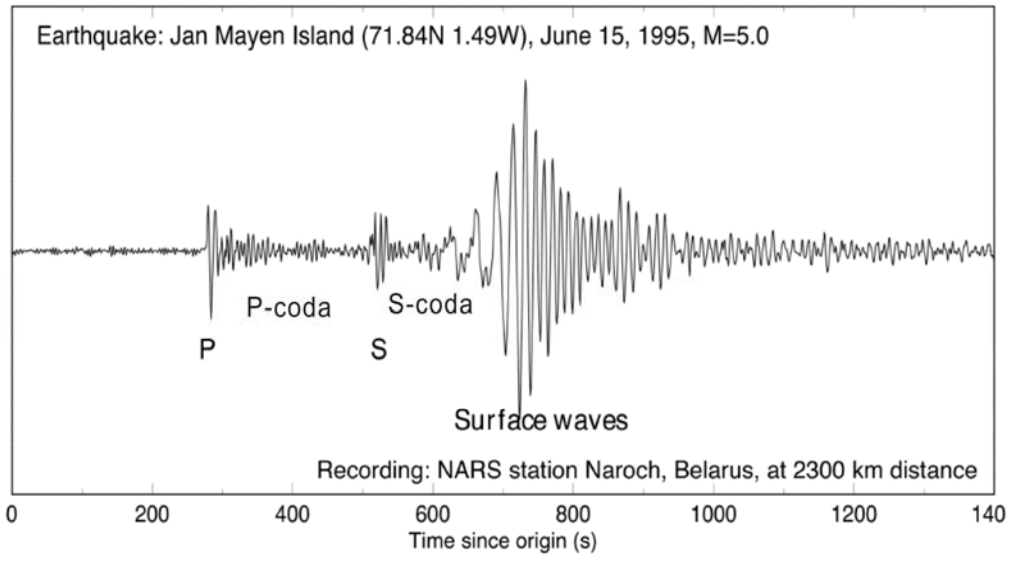

Figure 2-1. Sample seismogram of a local earthquake, showing P- and S-wave codas, recorded at NARS station Naroch, Belarus, at 2300 km distance. (Image from http://cosmos.ucdavis.edu/)

waves are considered, then '*P*-coda' denotes the train of waves located between the direct *P*- and *S*-waves, and '*S*-coda' corresponds to the waves following the direct *S*-waves (Sato et al., 1998) (Figure 2-1).

The interest in coda waves and the number of their detailed studies increased with the development of modern seismology. In this process, a big step forward was made by recognizing the lateral heterogeneity of the Earth and complexity of seismic wave propagation through the Earth. However, the development of concepts and applied methods in seismology is still influenced by the classical Earth model, which is mostly based on the assumption of a layered and laterally relatively uniform Earth (Herraiz et al., 1987).

Along with many geophysical, and particularly detailed controlled-source seismic studies (such as those using deep refraction and reflection experiments by modern seismic arrays), coda studies fill the broad gap between the real Earth and the lateral homogeneity assumption of seismological Earth models. Both geologists and geophysicists have ample evidence of the heterogeneity in the Earth's crust and the upper mantle down to about 100-200 km depths, which is usually called the lithosphere. From a broad geological point of view, it is clear that the Earth is heterogeneous on many scales. The Earth's crust contains a wide variety of rock types, and its composition changes on scales of a few millimetres to many hundreds and thousands kilometres. Tectonic processes also contribute to the heterogeneity within the lithosphere by means of faulting and folding. With growing understanding of the heterogeneous character of the lithosphere, the interaction of seismic waves with small obstacles, such as wedges, interfaces, etc, has been emphasized (Pilant, 1979). The observations of the effects of

scattering and attenuation were related to this inhomogeneity of the Earth. At the same time, Aki (1969) focused the attention on the later parts of local-earthquake seismograms, where the backscattered waves were likely to be dominant; this backscattered wavefield was the coda wavefield. Coda waves cannot be explained by deterministic structures imaged in tomographic or other methods in classical seismology, and they are considered as consisting of the superposition of many secondary waves generated by scattering of the primary waves on the spatially-distributed heterogeneities. Such observations were not explicable without accepting lateral heterogeneity, and they became the key evidence during the early 1960's, when more accurate data were obtained.

The new coda and attenuation observations were difficult to explain by using the classical, arrival-based seismic analysis procedure. It was urgently needed to develop new methods specially designed to work with seismic waves in a laterally heterogeneous Earth. At the same time, a good understanding of scattering and attenuation processes was required as a basis for the new methodology (Herraiz et al., 1987).

It is well-known that short-period (1-10 Hz) waves have high sensitivity to the shallower lithosphere. Applying these seismic waves to studies of source parameters of local earthquakes and source/receiver site effects made the need for heterogeneous Earth models more urgent (Espinosa, 1968, 1969, 1971; Espinosa and Algermissen, 1972a, b, 1973; Bard and Gariel, 1986). Unfortunately, this sensitivity also contributes to the uncertainty of short-period studies, because of the complex nature of lithospheric heterogeneities. Removing these complicating effects in order to extract the path and source information is a difficult but particularly important goal.

Constraining the lateral heterogeneity in a conventional, deterministic way may be impractical because of the large number of parameters involved and limited data available. Statistical techniques were introduced by several seismologists, and such methods were viewed as providing viable solutions. With these methods, only a small number of statistical parameters were required to describe the distributions of heterogeneities within the Earth. This work began in the late 1960's and early 1970's by using explosion data (Wesley, 1965; Nikolayev, 1968; Nikolayev and Tregub, 1970; Levin and Robinson, 1969; Greenfield, 1971), teleseismic records (Haddon, 1972; Cleary and Haddon, 1972), and lunar seismograms (Nakamura *et al.,* 1970; Dainty *et al.,* 1981).

Aki (1969) pioneered the application of statistical descriptions to high-frequency (>1Hz) seismic records by focusing the attention on the wave trains of local earthquake seismograms. Array observations have shown that such wave trains were not regular plane waves coming from the epicentre but composed of waves coming from all directions. Aki et al. (1969) showed that these waves could originate from randomly distributed heterogeneities having random sizes and contrasts of physical properties and suggested a description of the Earth as random medium with a broad spectrum of spatial velocity fluctuations. This model is broadly accepted to the present day, and it is commonly used to describe coda wavefields and short-scale lithospheric heterogeneity.

2.2 Applications of coda wavefield studies

Many seismic studies address properties of the seismic coda from earthquakes and explosions, and in particular, its amplitude decay and attenuation. Short-period coda

amplitude decays lead to the most stable estimates of source magnitudes (Phillips et al., 2004), and coda attenuation is often related to crustal properties that are difficult to measure otherwise (Aki and Chouet, 1975). Because coda waves can be considered as the superposition of many independent events, and are independent of epicentral distance, coda wave analysis is a useful tool for separation of source and path effects in the coda power spectrum values, and for obtaining the relationships between the coda power spectrum and crustal properties. It is widely used to study the important parameters of the seismic source (such as magnitude), the effects of the medium on wave propagation, and even station-site effects. For the wave-path part, the amplitude decay of coda wave is an efficient method for extracting important information about the structure of the Earth. High-frequency (>5 Hz) *P*-wave codas from PNEs in the East European Platform also led several researchers (Ryberg et al., 1995; Enderle et al., 1997; Morozov et al., 1998a,b; Ryberg and Wenzel, 1999; Morozov, 2001) to propose insightful yet sharply contrasting models of small-scale heterogeneity of the uppermost mantle.

Because coda waves originate from random processes, they can be statistically analyzed. Moreover, the great variety of paths traveled by these waves provides information concerning the average properties of the medium instead of just the characteristics of a particular path. Thus, coda wave analysis provides a reliable way to estimate the important averaged parameters quantifying the seismic source radiation and receiver-site amplification, both of which are used in seismic risk assessment. It also allows the investigation of propagation effects, and the important information about the structure of this region is provided as well.

The two medium parameters that are commonly obtained from coda studies are

the attenuation quality factor Q, and the backscattering coefficient (scattering amplitude). In our research, we focus on the coda wave quality factor Q, and particularly on its apparent frequency dependence.

In the past decades, the Q value has been extensively studied in many regions around the world (e.g., Herraiz M. et al.,1987; Canas et al., 1988; Zelt et al., 1999; Morozov, et al., 2000; Wong et al., 2001; Yun et al., 2007; Morozov, 2008a, 2009) and proven to be extremely sensitive to the geological environment. For example, in general, Q was found to be lower in tectonically active regions and higher in stable regions. Furthermore, several reports suggesting changes in Q as a precursor to earthquakes were published (e.g., Sato, 1986). Note that in the mid-1980s, there were significant criticisms of such results (e.g., Sato, 1988), although many studies still indicated a positive correlation between temporal change in coda characteristics and the occurrence of large earthquakes. Among the most serious criticisms were the possible effects of using different lapse times, earthquake focal regions, and differing focal mechanisms to establish the temporal change in coda characteristics for different earthquakes (Sato and Fehler, 1998).

Table B-1 (Appendix B) gives my compilation of the frequency-dependent coda Q data in the commonly used form $Q(f) = Q_0 f^{\eta}$ (Aki and Chouet, 1975) obtained by different authors employing the coda-wave analysis. These results can be considered well-established and cover broad areas of the world.

As shown in Table B-1, the related information in some areas is incomplete, while in most cases, the reported coda $Q(f)$ increases with frequency. Parameters Q_0 and η

correlate with tectonic types, with higher Q_0 and lower η corresponding to stable (i.e., older and colder) areas. The latter observation was initially made by Aki (1980) and further corroborated in many studies.

Note that the observed $Q(f)$ still does not necessarily mean that the Q of crustal material is frequency-dependent. As in other Q studies, the coda $Q(f)$ dependence is apparent (Aki, 1980), and the dependence on frequency may be related to the dependence of Q on the depth at which scattering occurs (e.g., Aki and Chouet, 1975). Such apparent frequency dependence could be explained if the coda waves at 1 Hz were primarily composed of surface waves scattered from shallow heterogeneities, and those at the higher frequency band were primarily backscattering body waves from the deep, high-Q lithosphere (Aki and Chouet, 1975). However, Morozov (2008a, 2009) recently took a much stronger view on this apparent frequency dependence and showed that it could be completely spurious and caused by inaccurate assumptions about the uniform "background" Earth structure. I will discuss these points in detail in the following chapters of this thesis.

2.3 Mechanisms and measurement of attenuation

As we know, when sound travels through a medium, its intensity decreases with distance because of the dissipation of the acoustic energy (Figure 2-2). The same energy loss occurs when the seismic wave propagation through a real Earth medium. This phenomenon is referred to as attenuation.

Scattering and absorption of high-frequency seismic waves frequently occur as combined processes, and they provide important parameters to quantify and physically characterize the medium. The attenuation of short-period (>1Hz) seismic waves is extremely important in understanding the physical laws according to which the elastic energy of an earthquake propagates through the Earth, and especially through its lithosphere. As mentioned above, when a seismic wave travels through an idealized medium, the amplitude is only reduced by the spreading of the wave; however, the amplitude decay of seismic wave during its propagation through the Earth is not only caused by geometrical spreading, but also by scattering due to heterogeneities and intrinsic absorption or anelasticity. The combined effect of scattering and absorption is called attenuation. Attenuation is usually expressed by the dimensionless quality factor Q^{-1}:

$$Q = 2\pi \frac{E}{\Delta E} \ , \tag{2-1}$$

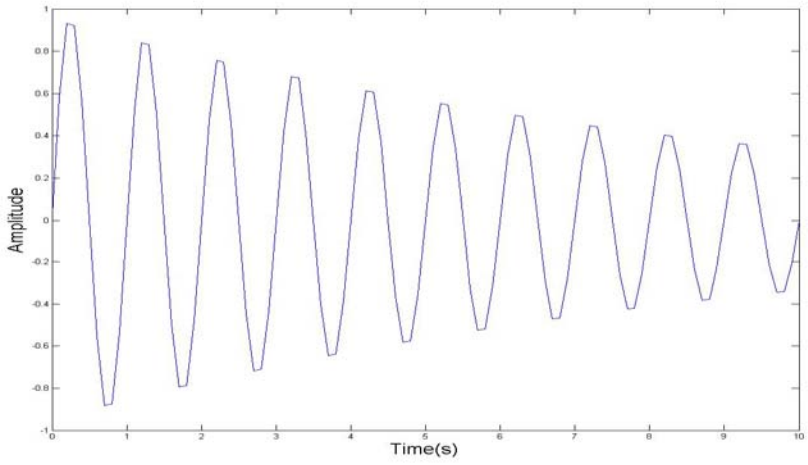

Figure 2-2. A sketch of sine-wave amplitude decaying or “attenuating” with time

where E is the energy in a seismic wave, and ΔE is the energy dissipation after one period of oscillation (Aki and Richards, 2002). Therefore, the larger values of quality factor Q are, the lower is the attenuation.

Two distinct mechanisms of seismic wave attenuation are recognised, both of which contribute to the properties of coda Q. These mechanisms are: 1) elastic attenuation associated with wave scattering, and 2) anelastic, or intrinsic attenuation caused by absorption of seismic energy. These mechanisms have distinct physical characteristics and often show characteristic dependencies of Q on the frequency.

The intrinsic absorption within the lithosphere describes conversion of vibration energy into heat, and the loss of seismic energy due to internal friction such as damping by fluids in cracks and pores or friction along grain boundaries. It is denoted by an intrinsic Q_i value. Conversely, scattering attenuation due to distributed heterogeneities redistributes wave energy within the medium. It transfers wave energy to later arrivals or to other propagation directions, and its magnitude depends on the scales of heterogeneities. However, for relatively weak and small-scale scattering, its effects can also be described by quality factor Q_s.

Scattering is a very complex process depending on various properties of the background lithospheric structure and of the wavefield. In most cases, scattering is also believed to be responsible for the observed steep increase of $Q(f)$ with frequency (e.g., Aki and Chouet, 1975), and therefore this mechanism needs to be specially considered.

Seismic scattering describes the deviation of elastic wave energy from its general propagation direction, and it is the process in which a primary wave interacts

with 3-dimensional heterogeneity of the medium and produces new secondary waves. Since scattering has the same observational effect as anelasticity, namely a reduction of the amplitude, it can also be described by a quality factor *Q*, which depends on the spatial structure of the scattering heterogeneities in the medium, on the size of the velocity and density fluctuations (Aki and Chouet, 1975).

The characterization of the Earth as a random medium is complementary to the classical model of a stratified medium. It seems to imply the following three aspects. First, it implies wave phenomena in a medium of three-dimensional heterogeneity rather than a medium which varies with depth only. Second, it implies relatively rough heterogeneities rather than smooth ones, which would be reflected by classical deviations of the primary wave paths in the form of refraction and/or reflection. Finally, it implies an incoherent signal rather than a coherent one (Aki, 1982). Here, the term 'rough' corresponds to the heterogeneity scale-length that is comparable or shorter than the seismic wavelength involved.

Correlation distance can be used to describe the heterogeneity scale-length, which expresses the separation at which fluctuations become uncorrelated in the statistical study. Assuming that the wavelength is much shorter than the travel distance, then for wavelengths either much greater or shorter than the sizes of heterogeneities, the medium can be regarded as homogeneous or piecewise-homogeneous (as Figure 2-3, top). In this case, the waves are not affected by the obstacles and the medium acts like a homogeneous body. When the wavelength is comparable to the heterogeneity scale-length or somewhat greater, scattering can become strong (Figure 2-3, bottom). This case is very common in many seismological situations. When the scale of heterogeneities

becomes much smaller than the characteristic wavelength, the high-frequency components are lost because of destructive interference (Marion and Coudin, 1992).

Two different types of scattering during wave propagation in a heterogeneous medium are differentiated according to the direction of the scattered energy produced: forward and backward scattering. Forward scattering refers to most of scattered energy being sent forward in the incident primary wave direction, and with backward scattering, the energy is deflected backward. Impedance (density times velocity) fluctuations tend to introduce mainly backscattering, while velocity perturbations without impedance variations create forward scattering. However, in both cases, the results also strongly depend on other factors, such as the scale-lengths, relative signs of anomalies, and types of the incident waves.

The scattering strength may be different in different media and for different types of

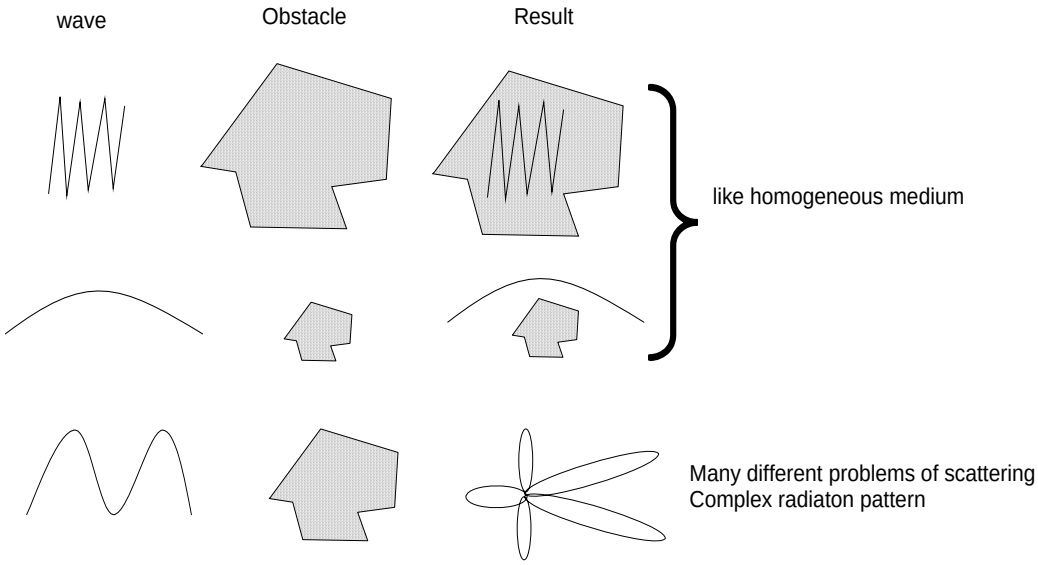

Figure 2-3. Simplified schematic of the relation between wavelength sizes and heterogeneity scale-length shown as schematic obstacles, modified from Herraiz et al. (1987).

incident waves. In a quasi-homogeneous medium, with only sparse heterogeneities present, it should be sufficient to only consider individual wave-scatterer encounters ('single scattering'). If scattering is strong, it may be necessary to consider 'multiple scattering', when multiple scattering events take place before the coda wave is recorded. If the scattering is strong enough, it could also be viewed as a diffusion process.

In the case of relatively weak scattering, scattering strength can be described by the turbidity coefficient:

$$g = \frac{\Delta I}{IL} = \frac{1}{\ell}. \tag{2-2}$$

Here, ΔI represents the loss of energy by scattering when a wave of intensity (energy per second and per unit area) I passes through a layer of thickness L, and ℓ is the 'mean free path'. Thus, if g is much less than 1/(travel distance from the source), it is not necessary to consider multiple scattering. The discrimination between weak and strong scattering process can be made considering if the ratio $\frac{L}{\ell}$ being small or not.

The Born's approximation is scattering analysis method in inhomogeneous media based on the first-order perturbation, and it neglects both the loss of energy from the primary waves and multiple scattering (Born and Wolf, 1965). Although this approximation is violates the energy conservation law, it has been accepted in various physical problems. The Born's approximation can only be used for weak scattering. In seismic wave analysis at high frequencies, the Born's approximation is often used to explain the coda wave decay or to invert for attenuation parameters of seismic waves. In the present study, Born's approximation is the basis of numerical modeling.

2.4 Separation of Q_i and Q_s

Coda wave analysis can be a useful tool for distinguishing between the two contributions to attenuation (Gao, 1984). Dainty (1981) summarized this approach by the following relation:

$$\frac{1}{Q} = \frac{1}{Q_i} + \frac{1}{Q_s} \ , \tag{2-3}$$

where Q is the total quality factor obtained by experimental measurements based on the decay of seismic waves; Q_i^{-1} considers the intrinsic absorption and Q_s^{-1} represents the attenuation due to scattering. In a theoretical analysis of scattering, parameterization (2-3) was used by Dainty (1981), who showed that at 1-30 Hz, the observed Q of S waves could be best described by the following expression (Warren, 1972):

$$\frac{1}{Q} = \frac{1}{Q_i} + \frac{gv}{2\pi f} \tag{2-4}$$

where v is the velocity, g is the turbidity, and f is the frequency of the wave under consideration. Note that by comparing eqs. (2-3) and (2-4), one can see that if g is constant, Q_s should be proportional to the frequency. Such dependencies were often observed and considered characteristic of scattering on larger-scale structures (Dainty, 1981). Recently, Padhy (2005) also utilized this parameterization to describe the attenuation of high-frequency scattered *Lg* and *S* waves.

To distinguish the two contributions to $1/Q$, distance-dependent coda amplitude analysis is an effective tool (Gao, 1984; Wu, 1985). In several forms of this method, the amplitude increase observed at ~20 - 70 km from an earthquake source is interpreted as caused by backscattering, and by means of complex Monte-Carlo numerical modeling,

both the Q_i and Q_s values are estimated. However, as Morozov (2008) argued, such complex modeling always relies on simplifying assumptions about the geometrical spreading of the wavefield. All $Q_i - Q_s$ separation studies and most studies in which frequency-dependent $Q(f)$ is reported are based on assumptions of a uniform "background" lithospheric model, which are very far from reality. As Morozov (2008) showed, when such an assumption is removed, the attenuation data can typically be interpreted by using a frequency-independent "effective" attenuation Q_e. The absorption and small-scale scattering components of this Q_e (eq. 2-3) may not be distinguishable from the available data.

Thus, the question of whether scattering and absorption can be separated in coda or other seismological data remains open. Until now, the question of their separability lies in the realm of theoretical models, assumptions, and numerical models. By contrast to such model-based approaches, in this thesis and following Morozov (2008), I undertake an empirical approach and focus on attenuation characteristics that can be measured without simplifying or theoretical assumptions. The numerical modeling performed below aims at reproducing and inverting the coda parameters that are unambiguously derived from the PNE data.

2.5 Methods of coda *Q* measurement

Several methods for measuring anelastic properties of the Earth have been developed. Q values can be estimated from seismic amplitude decay (Braile, 1977; Brzostowski and McMechan, 1992; Grad and Luosto, 1994), amplitude rise times (Gladwin and Stacey, 1974), pulse broadening (Wright and Hoy, 1981), spectral ratio methods (e.g., Bath, 1974; Carpenter and Stanford, 1985), common spectrum method

(Halderman and Davis, 1991; Gao, 1997; Morozov et al., 1998b), wavelet modelling (Jannsen et al., 1985; Matheney and Nowack, 1995; Matheney et al., 1997), and analytical signal methods (Taner et al., 1979). Jennsen et al. (1985), Badri and Mooney (1987), Tonn (1989), and Matheney and Nowack (1995) compared different techniques and found that each of these methods works well in favourable situations while some of them have significant limitations. In particular, amplitude-decay based techniques strongly depend on the correct evaluation of the geometric spreading effects; pulse broadening and rise-time approaches are often source-dependent (Blair and Spaths, 1984). By contrast, spectral ratio methods and related techniques employing instantaneous wavelet attributes are less affected by focusing and source signatures, yet they may be sensitive to data noise. White (1992) critically examined the accuracy of estimating Q from VSP seismic data.

In application to coda Q measurements, only two of the above techniques are used: the spectral-ratio and amplitude-decay methods. In the spectral-ratio method, the following model for seismic amplitude is employed:

$$u(f,t) = S(f)R(f)G(t)\exp\left(-\frac{\pi f}{Q}t\right), \tag{2-5}$$

where $u(f, t)$ is the amplitude spectrum of the seismic phase recorded at propagation time t, $S(f)$ is the source spectrum, $R(f)$ is the combined recording-site and receiver responses, and $G(t)$ is the geometrical spreading. Because the exponential attenuation factor is the only factor depending on both the frequency f and time t, it can be isolated by taking logarithms of the spectral ratios of the amplitudes recorded at two different times t_1 and t_2:

$$\log \frac{u(f,t_2)}{u(f,t_1)} = c - \frac{\pi(t_2 - t_1)}{Q} f \,, \tag{2-6}$$

where $c = \log(G(t_2)/G(t_1))$ is independent of f. Therefore, the log-spectral amplitude ratio should exhibit a linear dependence on f, from whose slope the value of Q^{-1} can be determined.

For significant separation between the measurement times, the spectral ratio method (2-6) is most robust and reliable; however, it only works for frequency-independent attenuation estimates. If frequency-dependent Q-factor is of interest, then the only usable method is the amplitude-decay method (Braile, 1977). In most studies using this technique, the following model for seismic wave (including coda) amplitude is used:

$$A(t, f) = A_0(f) t^{-\zeta} \exp\left(-\frac{\pi f}{Q(f)} t \right) , \tag{2-7}$$

where t is the observation time, f is the frequency, $A_0(f)$ represents the source spectrum, and $t^{-\zeta}$ describes the geometrical spreading. Typically, it is assumed that the geometrical spreading is known with good accuracy. In the case of coda waves, this factor represents the geometrical spreading which is not compensated by the scattering volume increase with coda lag time. Usually, values of 0, ½, or 1 are used for ζ (Aki, 1980), although Frankel et al. (1990) showed that it could also be variable within different regions. For the far-regional and teleseismic PNE codas considered in this study, $\zeta \approx 0$, corresponding to an approximation of coda waves with cylindrical propagation symmetry (i.e., consisting predominantly of surface or guided waves) and generated near the surface (Morozov and Smithson, 2000).

If the geometrical factor is known, it can be compensated by multiplying eq. (2-7) by t^{ζ}. After such compensation, by taking the natural logarithms, one obtains a linear dependence of ln$A$ on t:

$$\ln\left[A(t, f)t^{\zeta}\right] = \ln C(f) - bt \ , \tag{2-8}$$

where $C(f)$ denotes the limit of $A(t,f)t^{\zeta}$ at $t \to 0$, and the negative coda-amplitude slope is $b = \frac{\pi f}{Q(f)}$. Note that, because eqs. (2-7) and (2-8) show a linear decay of ln$A$ with propagation time, they are not suitable in strong-scattering cases.

From time-domain coda slopes measured from the data, relation $Q = \pi f/b$ gives the desired Q. This approach is used in most existing attenuation studies in which $Q(f)$ is sought. If b is not strictly proportional to f, Q becomes frequency-dependent, which appears to be commonly observed. However, not all seismologists agree that the geometrical spreading can be sufficiently accurately compensated (i.e., $C(f) \neq 1$) in eq. (2-8), and an incorrect compensation could lead to strong apparent frequency dependence in Q (Morozov, 2008a). In the following, I review the detailed arguments about the dependence of coda Q on frequency.

2.6 The argument about the frequency-dependence of *Q*

Despite widespread observations of frequency-dependent coda-, body-, and surface-wave attenuation, the causes of these frequency dependencies are still not well understood. Frequency-dependent Q values are commonly presented in a power-law form:

$$Q(f) = Q_0\left(f \Big/ f_0\right)^{\eta}, \tag{2-9}$$

where f_0 is some reference frequency often taken to equal 1 Hz, and Q_0 is the value of Q at this frequency (Aki and Chouet, 1975). Notably, in most cases $Q(f)$ increases with the frequency ($\eta > 0$), and large values of $\eta \sim 0.5$ - 1 are not uncommon in surface waves, *Lg Q* and *Lg* coda Q , and deep borehole studies (e.g., Nuttli, 1973; Hasegawa, 1985; Der et al., 1986; Campillo, 1987, 1990; Steensma and Biswas, 1988; Benz et al., 1997; Mandal and Rastogi, 1998; Frankel et al., 1990; McNamara et al., 1996; Mitchell and Cong, 1998; Mitchell et al., 1997, 1998; McNamara, 2000; and Erickson et al., 2004). Such an increase is somewhat counter-intuitive, considering that the observed abundance of heterogeneities is usually greater at shorter scale-lengths. Positive frequency dependence of $Q(f)$ at short periods led Aki (1980) to advancing the absorption-band hypothesis, and the strong drop in the observed η values near 10-Hz frequencies was described as the "10-Hz transition problem" (Abercrombie, 1998). Visco-elastic rheological models of Earth materials (Liu et al., 1976) and scale-length selective distributions of scale-lengths of scatterers within the crust (e.g., Sato, 1990; Sato and Fehler, 1998) were proposed to explain the observations of the frequency-dependent $Q(f)$, and the apparent character of this property and its sensitivity to the underlying wavefield models have also been long recognized. Worldwide data compilations (see Table B-1 in Appendix B) suggest that active tectonic regions are generally characterized by low Q_0 and high η, while stable cratons – by higher Q_0 and lower η (e.g., Aki, 1980; Steensma and Biswas, 1988; Benz et al., 1997; Mandal and Rastogi, 1998; Erickson et al., 2004). However, in the PNE studies in the Siberian Craton, extremely high values of $\eta \approx 1$ were also found in combinations with high Q_0 (Morozov et al., 2006), which appeared to be in conflict with the above trend for stable areas.

The contradiction above indicates the need for re-examining the causes of the $Q(f)$ dependence, and for this we need to look at the original observations. Note that for $\eta \approx 1$, the amplitude decay rate with time becomes frequency-independent in eq. (2-7). This means that the amplitude decay is purely geometrical, which potentially could represent scattering on large-scale structures suggested by Dainty (1981). If the observed increase of apparent $Q(f)$ with frequency is caused by geometrical spreading, then in general, observations of $\eta > 0$ could in fact be related to lower intrinsic attenuation ($Q > Q_0$) combined with significant uncompensated geometrical effects (i.e., inaccurately compensated geometrical spreading in eq. 2-8).

The power-law dependence (2-9) is generally dictated by convenience and assumptions about the scaling and symmetry properties of the wavefield (via factor $t^{-\zeta}$ in eq. (2-7)). Although in many cases this dependence allows fitting the observations, the acute sensitivity of parameters (Q_0, η) to the assumed values of ζ is also well known (e.g., Kinoshita, 1994; Adams and Abercrombie, 1998). As I show below, by exploiting this sensitivity, this ambiguity can be removed and explained by geometrical effects. Interestingly, this will also lead to the removal of the frequency dependence of Q.

Compensation of geometrical spreading in equation (2-7) may be relatively accurate for deeper, local earthquake codas involving straight scattered rays and uniform scattering volumes (Aki and Chouet, 1975). However, at shallow depths, crustal-scale and regional distances, scattering tends to concentrate near the surface, and scattered waves consist of complex assemblages of diving, refracted, reflected, guided, and surface modes. Based on various assumptions about these modes and stochastic properties of the crust, several coda models can be used (e.g., Aki and Chouet, 1975; Sato and Fehler,

1998). However, in practice, empirical distance and spectral corrections are still required for virtually any model (Mayeda and Walter, 1996; Phillips et al., 2004). Here, we introduce such a correction by noting that an unknown, uncompensated "geometrical attenuation" $G(t)$ should be present in the coda (Morozov, 2008):

$$A(t, f) = A_0(f) t^{-\varsigma} G(t) \exp\left(-\frac{\pi f}{Q(f)} t\right). \tag{2-10}$$

The geometrical attenuation factor $G(t)$ includes both uncompensated geometrical spreading and scattering (elastic attenuation Q_s above; Dainty, 1981). Because these two contributions can only be separated based on a detailed, well-constrained wave propagation model, such separation could be very difficult for most observations. Nevertheless, for empirical coda characterization, we combine these two factors together in a single effective geometrical attenuation function $G(t)$.

Because with typical datasets it is only practical to seek a two-parameter coda description (similarly to (Q_0, η) in equation (2-9)), we abandon the frequency dependence of Q by setting $Q(f) = Q_e$ in relation (2-8) and approximate $G(t)$ as $\exp(-\gamma t)$, obtaining (Morozov et al., 2008):

$$A(t, f) = A_0(f) t^{-\varsigma} \exp\left[-\left(\gamma + \frac{\pi f}{Q_e}\right) t\right], \tag{2-11}$$

where the geometrical attenuation (relaxation) parameter γ is measured in units of 1/*time*. Note that the case of $\eta = 1$ ($Q \propto f$ in equation (2-7)) simply corresponds to a non-zero γ and low intrinsic attenuation ($1/Q_e = 0$) in relation (2-11).

In his theoretical analysis of scattering of 1-30-Hz *S* waves, Dainty (1981) used

model (2-11) in the form of equation (2-4), in which $g=2\gamma/v$. . Dainty (1981) concluded that if larger scatterers dominate the scattering, g can be considered constant. Note that for seismic coda, such larger scatterers could effectively be represented by strong velocity gradients, faults, the Moho, sedimentary boundaries, and other crustal structures affecting the propagation of scattered coda waves.

Thus, it appears that the (Q_0, η) description of frequency-dependent coda attenuation (and maybe also in other types of crustal Q) can be effectively replaced with (γ, Q_e). Several advantages arise from such a replacement:

1) Formulas (2-10) and (2-11) do not rely on wavefield models and assumptions about geometrical spreading or scattering but empirically parameterize them instead;

2) Geometrical attenuation and Q_e are explicitly separated; and

3) Q_e becomes frequency-independent, in agreement with the simple Newtonian solid-state mechanics and at least within the presently available data resolution.

4) The puzzling increase of coda $Q(f)$ with frequency (Table B-1) seemingly suggesting depletion of scatterers at shorter scale-lengths becomes explained by geometrical attenuation due to reflected (among other) scattered waves.

5) The geometrical model (γ, Q_e) also appears to alleviate the "10-Hz transition problem" (Abercrombie, 1998) and provides a new perspective on the absorption-band hypothesis (Morozov, 2008a, 2009).

6) Most importantly, as demonstrated by a worldwide compilation of (γ, Q_e) values (Morozov, 2008 and Table B-1) and by examples from PNE profiles given in this

thesis, parameter γ appears to be relatively stable across large areas and correlates with tectonic types and ages. By contrast, Q_e shows strong variability, particularly within the active-tectonic regions (Morozov, 2008a).

Therefore, in the following, I use the (γ, Q_e) model as the primary description of attenuation in this study.

2.7 *Q* model of this study

Because of its combining numerical experiments with data observations, three different types of Q values need to be carefully differentiated in this study. First, the intrinsic crustal attenuation describes the loss of seismic energy within the crust, caused by internal friction, friction along grain boundaries, and damping by fluids in cracks and pores. Weak, small-scale scattering may also contribute to this attenuation; however, this contribution is indistinguishable from the effects of the intrinsic Q in neither our modeling nor measurements. The intrinsic attenuation is described by intrinsic Q_P and Q_S values corresponding to the *P*- and *S*-wave energy dissipation during one wave cycle, respectively (Aki and Richards, 2002). For simplicity, we only test crustal models with proportional values of Q_P and Q_S. The second type is our empirical frequency-independent quality factor Q_e obtained by applying eq. (2-11) to the spectral-slope measurements. The third type of Q is the observed apparent coda quality factor, $Q_{coda}(f)$. It is based on the same time-frequency amplitude model (2-8), in which ζ is set equal to the theoretically-expected level of 0, and $C(f)$ is assumed to equal 1:

$$Q_{coda}(f) = \frac{\pi f}{b} \quad , \tag{2-12}$$

where slope b is measured from the natural logarithm of the seismic trace envelope. This type of Q is mostly used for comparison with other studies.

Note that in the absence of attenuation ($1/Q = 0$) and incomplete geometrical compensation ($\zeta \neq 0$, or $C(f) \neq 1$), b would be non-zero. Therefore, it is reasonable to assume that the coda slope b varies with frequency, starting from a (generally) non-zero value at $f = 0$:

$$b = \gamma + \frac{\pi f}{Q_e}. \tag{2-13}$$

Consequently, the expressions above lead to a new model for the apparent frequency dependence in coda $Q_{\mathrm{coda}}(f)$:

$$\frac{1}{Q_{coda}(f)} = \frac{\gamma}{\pi f} + \frac{1}{Q_e}. \tag{2-14}$$

In this study, I compare the (Q_0, η)- and (γ, Q_e)-type models of coda attenuation by using numerical examples and by inverting real PNE coda amplitudes. Below, I generate four finite-difference models of PNE coda wavefields resulting from realistic crustal and upper-mantle velocity models and test them for variations of velocities and Q within the crust. As expected, the (Q_0, η) model leads to strong spurious coda $Q(f)$ dependencies. Inversion of this $Q(f)$ for the true crustal attenuation could represent a non-trivial task. By contrast, in the (γ, Q_e) model, the values of γ can be predicted from the crustal structures by numerical wavefield modeling. Coda Q_e can be related to the average S-wave Q_S of the crust, assuming its proportionality to the P-wave quality factor Q_P. Wavefield modeling performed for several types of velocity structures allows us to

construct "calibration" dependences $Q_S(Q_e)$, by using which the crustal Q_S could be estimated from coda Q_e measurements. In addition, a detailed development of the (γ, Q_e) interpretation, correlation with tectonic types and ages, and comparison to a number of borehole, *Lg*, and coda *Q* studies was presented in Morozov (2008a).

3 MODELLING P-WAVE CODA OF PNE ARRIVALS

Morozov and Smithson (2000) performed trace-envelope measurements in Quartz PNE records for a teleseismic *P*-wave coda. Although these authors used only two frequency values, the results suggested a strong apparent frequency dependence of $Q_{coda}(f) \approx 270f^{0.3}$, where f was expressed in Hz. These estimates were within the range of expected crustal-average Q_S values and therefore supported the association of the coda with L_g waves scattered within the crust. Here, I attempt to improve this estimate by using numerical modeling to derive a $Q_e(Q_S)$ dependence and re-interpret the observed $Q_{coda}(f)$ in terms of a frequency-independent Q_e and γ.

Below, I examine the effective frequency dependence of coda attenuation by numerical modeling the teleseismic *P* wave coda resulting from scattering of seismic energy from near-surface crustal heterogeneities. The use of near-surface crustal scatterers simplifies our computations, and it is also justified by the increased heterogeneity of the shallow crust and supported by several array observations (e.g., Greenfield, 1971; Dainty, 1985 and 1990; Bannister et al., 1990; Gupta et al., 1991) and previous coda modeling (Dainty and Schultz, 1995). The choice of the *P*-wave coda is due to several reasons (Morozov and Smithson, 2000): 1) *S*- and L_g phases are less pronounced in the PNE records; 2) their codas lie on top of the *P*-wave coda, complicating the observation and requiring their decomposition; and 3) because it propagates much slower, L_g phase is significantly more difficult to model accurately. Similarly, the Rayleigh wave (R_g) is not examined here because it decays quickly in near-

surface sediments and is not viewed as a significant factor in coda formation (Dainty, 1985). R_g is also not observed beyond ~200 km in PNE records. Finally, the use of *P*-wave coda at offsets of ~2900-km provides a sufficient coda time window before the onset of the *S* wave.

Our scattering model is based on Born's single-scattering, in which we consider the coda as a superposition of waves back-scattered from numerous discrete scattering sources. Each wave is due to a single scatterer in the absence of the other scatters. This weak scattering means the fluctuations of perturbed parameters are small when compared with their corresponding mean values. In this model, the fractional energy loss from primary waves is small, and it is possible to apply Born's approximation, in which the loss of energy from the primary waves as well as the multiple scattering are neglected.

To fully address the crustal scattering problem, 3-D modeling of crustal features including faults, mountain ranges, basins, shorelines, and topography is required. However, full 3-D modeling is still not practical at this time due to limited knowledge of the structural detail and scattering properties of the crust. Instead, we use a heuristic simulation of teleseismic *P*-wave coda amplitude decay modeled as scattering from heterogeneities near the Earth's surface, by combining 1-D reflectivity synthetics with the Born approximation of coda intensity. As this is not a 3-D crustal model, it cannot provide a completely realistic picture of the resultant coda decay; however, it captures the key mechanism of coda generation, provides improved estimates of crustal attenuation, and elucidates the problem of frequency-dependent $Q_{\mathrm{coda}}(f)$.

3.1 Numerical Coda Model

The scattering model represents crustal heterogeneities as point scatterers distributed within the Earth's crust. The resultant coda intensity (energy density) U recorded at a receiver at time t is an integral over volume V containing all scatterers:

$$U(\vec{r},t) = \int dt_s \iiint_V d^3\vec{r}_s \Psi(\vec{r}_s) U_{source}(\vec{r}_s,t_s) G(\vec{r}_s,t_s;\vec{r},t) \quad (3\text{-}1)$$

,

where t_s is the time of the direct arrival at the scatterer, $\vec{r}_s$ represents the scatterer positions, Ψ is the scattering potential describing the amount of energy reflected at each scatterer, U_{source} is the seismic source function describing the energy density arriving at the scatterer from the source, and $G(\ldots)$ is the Green's function, describing the propagation of scattered energy from the scatterer to receiver. Each scattering point acts as a secondary source for seismic waves (Figure 3-1). The displacement field from this kind of simple scatterer source is the elastodynamic Green's function.

Because in this model the upper crust is assumed to be the primary contributor to the seismic coda, this volume integral is further replaced with a surface integral:

$$U(\vec{r},t) = \int dt_s \iint_S d^2\vec{r}_s \Psi(\vec{r}_s) U_{source}(\vec{r}_s,t_s) G(\vec{r}_s,t_s;\vec{r},t)\,. \quad (3\text{-}2)$$

This approximation also allows us to reduce the volume of simulations by considering only the surface-to-surface Green's functions and to use a near-surface source modeling algorithm.

The Green's function G is translationally invariant in time and space:

$$G(\vec{r}_s,t_s;\vec{r},t) = G(\vec{r}-\vec{r},t-t_s)\,, \quad (3\text{-}3)$$

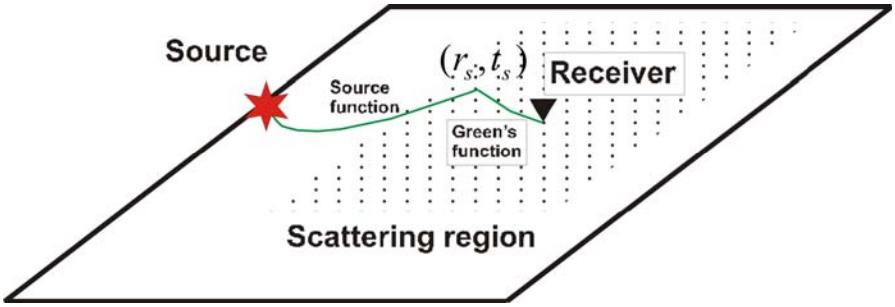

Figure 3-1. Near-surface scattering model (eq. 3-2). Seismic energy originates at the source, scatters from randomly and uniformly distributed surface points, and is detected at the receiver. The numerically-simulated Source and Green's functions describe the propagation of seismic energy (green lines).

and therefore:

$$U(\vec{r},t) = \int dt_s \iint d^2\vec{r}\,\Psi(\vec{r}_s) U_{source}(\vec{r}_s, t_s) G(\vec{r}-\vec{r}_s, t-t_s)\,. \tag{3-4}$$

For a given coda time t and velocity $v = \dfrac{|\vec{r}-\vec{r}_s|}{|t-t_s|}$ chosen for a particular scattered mode (e.g., v = 2.9 - 3.5 km/s for a scattered L_g), the contributions of scattered energy originate from an elliptical ring surrounding the receiver (Morozov and Smithson, 2000). The scattering area within the ring increases with time due to its increasing radius and partly compensates the energy decay due to the geometrical attenuation. For example, for a plane of constant scattering potential and no intrinsic attenuation, the coda energy would stay constant, provided that only surface-wave modes contribute to the Green's function (3-3).

In equation (3-2), by using the primary field as $U_{\text{source}}(\vec{r}_s, t)$, we only consider receiver-end scattering, similarly to how it was done in Morozov and Smithson (2000).

Due to reciprocity, the same coda should be produced by near-source scattering in the 1-D model. Dainty (1990) showed that this was also true in real records from Semipalatinsk nuclear explosions recorded at the NORESS array in Norway. In the single-scattering approximation of this study, the powers of the source- and receiver-end codas will add up, and the resulting dependence of coda slopes on the frequency should not change.

Inclusion of the near-source scattering would double the resulting singly-scattered coda intensity. However, in our approach, this intensity is controlled by factor Ψ in equation (3-4), which is set equal to a frequency-independent constant for simplicity. The value of this constant was established by matching the modeled coda amplitudes to those observed from PNE Quartz-4 (Morozov and Smithson, 2000; also see Chapter 5), and consequently it incorporates the contributions from both source and receiver areas. Therefore, the results of modeling using equations (3-2, 3-4) should be valid for single shallow scattering approximation of both near-source and near-receiver scattering.

3.2 Synthetic Green's function

Two dimensional, offset synthetic seismic sections were used as source and Green's functions for my scattering model later, and they were created using the reflectivity method (Fuchs and Müller, 1971) in several 1-D crustal and upper mantle models (Figure 3-2 & Tables 3-1, -2, -3, -4). The original FORTRAN program by K. J. Sandmeier was modified to handle large computations, parallelized, and incorporated into the IGeoS processing system by my supervisor (I. Morozov) allowing seamless filtering, inverting, saving, and plotting the results.

Computations were performed on a 66-processor 1.6-GHz AMD Opteron cluster and produced 800-second, 3-component synthetic records sampled at 20-ms intervals and output at 10-km intervals from near-zero to 3500-km distances from the source. Modeling frequency band was 0.2 – 20 Hz using a "delta-function" source function suitable for spectral measurements. The frequency band, listening times, and offset ranges were selected to cover the corresponding parameter ranges in PNE recordings (e.g., Morozova et al., 1999). Sufficiently dense phase velocity spectrum was selected in order to avoid frequency aliasing during numerical mode summations. As with any implementations of the propagator matrix method (Aki and Richards, 2002), all *P*/*SV* mode conversions and multiples were accounted for in the modeling.

I used four different velocity models to compute the synthetics (Figure 3-2 and

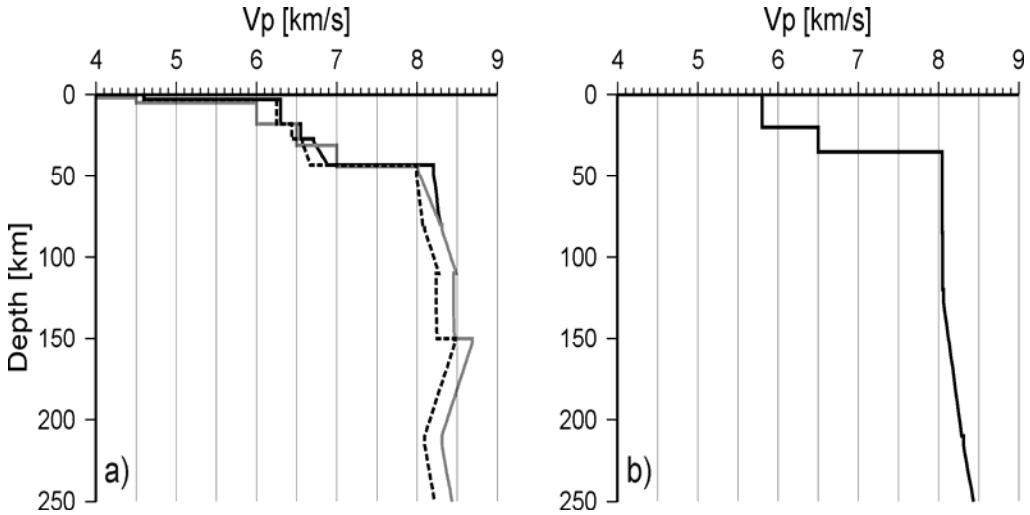

Figure 3-2. Upper 250 km of 1-D VP velocity models used in creation of synthetic seismograms. a) Models based on PNE Quartz results by Morozova et al. (1999): "Quartz" (solid black line), "Warm Quartz" (dotted black), and "Complex Crust" (grey); b) IASP91 model.

Tables 3-1, -2, -3, -4), including the global IASP91 model (Kennett and Engdahl, 1991) consisting of a simple three-layer crust and a mantle without strong gradients and low-velocity zones.

Table 3-1 "Quartz" velocity model

Depth(km)	Vp(above)(km/s)	Vp(below)(km/s)
0		4
3	5.2	6.2
18	6.4	6.5
27	6.6	6.7
43	6.9	8.2
80	8.3	8.3
110	8.5	8.45
150	8.47	8.7
210	8.3	8.3
410	9.03	9.36
660	10.2	10.97
871	11.25	11.25

Table 3-2 "Warm Quartz" velocity model

Depth(km)	Vp(above)(km/s)	Vp(below)(km/s)
0		4
3	5.185	6.185
18	6.31	6.41
27	6.465	6.565
43	6.685	7.985
80	8.085	8.085
110	8.285	8.235
150	8.255	8.485
210	8.085	8.085
410	8.815	9.145
660	9.985	10.575
871	11.0356	11.0356

Table 3-3 “Complex Crust” velocity model

Depth(km)	Vp(above)(km/s)	Vp(below)(km/s)
0		2.5
2	2.5	4.5
5	4.5	6.0
18	6.0	6.5
31	6.5	7.0
44	7.0	8.0
80	8.3	8.3
110	8.5	8.45
150	8.47	8.7
210	8.3	8.3
410	9.03	9.36
660	10.2	10.79
871	11.2506	11.2506

Table 3-4 IASP91 velocity model

Depth(km)	Vp(above)(km/s)	Vp(below)(km/s)
0		5.8
20	5.8	6.5
35	6.5	8.04
85	8.046	8.046
120	8.05	8.05
210	8.3	8.3
410	9.03	9.36
660	10.2	10.79
760	11.056	11.056

However, the IASP91 model is too slow for the platform areas of northern Eurasia, and the remaining three models were based on the detailed models derived from the PNE profile Quartz and considered the best match for the study area (Mechie et al., 1993; Morozova et al., 1999). The “Quartz” model contains a 3-gradient layer crust overlain by a 3-km-thick sediment layer and complex mantle with low-velocity zones at 110- and 210-km depths (Figure 3-2a and Table 3-1). Another, “Complex Crust” model has a high-contrast, 5-layer crust with a somewhat exaggerated attenuative layer (Q_S = 10) on its top and the Quartz mantle (Figure 3-2 and Table 3-2). Model “Warm Quartz” (3-2a) was an

attempt to simulate a high-heat flow regime in the Quartz model by applying a temperature-related negative velocity gradient within the crust (Christensen and Mooney, 1995). Note that compared to the IASP91 model, all three Quartz-based models show more complex waveforms containing crustal L_g phases in addition to the *P* and *S* phases (Figure 3-3). In order to collect data on the sensitivity of the results to the crustal velocities alone, I also repeated the Quartz simulations after applying ±5% perturbations of crustal velocities (Figure 3-2a).

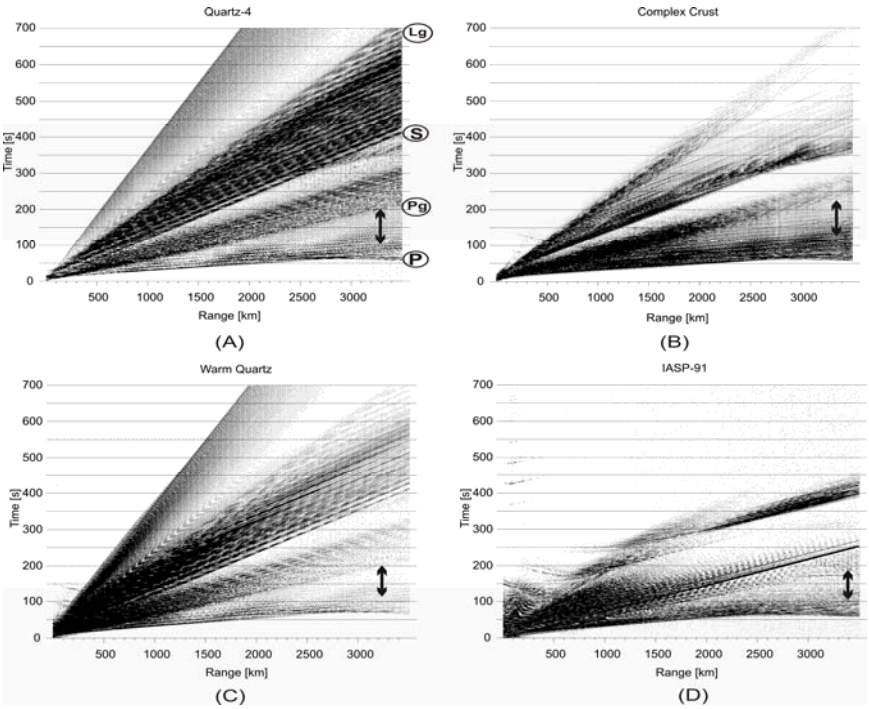

Figure 3-3. Reflection synthetic seismograms used as Green's functions, created by using the four different velocity models in Figure 3-2: a) Quartz-4, b) Complex Crust, c) Warm Quartz, and d) IASP91. Note the similarities between wavefields a-c), and their contrast with d). Arrows indicate the positions of the receiver and coda time ranges used in the analysis. The key regional phases are labelled.

Multiple simulations were performed for each model, with *P*- and *S*-wave quality factors for layers in the crustal part of the model set proportional: $Q_P = 2Q_S$, with values of Q_S ranging from 100 to 1000 to encompass the expected Earth's whole-crust Q_S values. This range of Q_S corresponds to *Lg Q* values of ~300-1000 measured from 19 Russian PNEs by Li et al. (submitted) and extended to low-*Q* values in order to investigate the crustal effects. Mantle attenuation in each velocity model was fixed by using the mantle Q_P values derived from *P*-wave Quartz PNE data. These Q_S values ranged from $Q_S = 750$ below the Moho to 600 above the 410-km discontinuity, with an attenuative zone of $Q_S = 200$ in the region of the Lehmann discontinuity at 110-150-km depths (Morozov *et al.*, 1998b).

3.3 Synthetic stochastic coda waveforms

As in Morozov and Smithson (2000), the *P*-wave coda was measured in this study at near-teleseismic, 2900-km offsets to allow a significant time interval for measurements before the onsets of P_g and *S* waves. Since L_g waves originating from the source (or L_g waves scattered near the source) travel too slowly to arrive within this time interval, the scattering region was assigned around the receiver only. The region size was chosen to be a 1200-km square on a side, allowing 600 km from the central receiver to the nearest edges (Figure 3-4). For scattered waves of 3-km/s (L_g) velocity, this gives a ~200-s window in which to reliably measure the coda amplitude decays. As the Q_S value in the reflectivity synthetics is constant throughout the crustal section, and crustal scattering does not depend on the source-receiver offsets, the receiver's offset value should not influence $Q_{coda}(f)$ and Q_e values measured from the output traces.

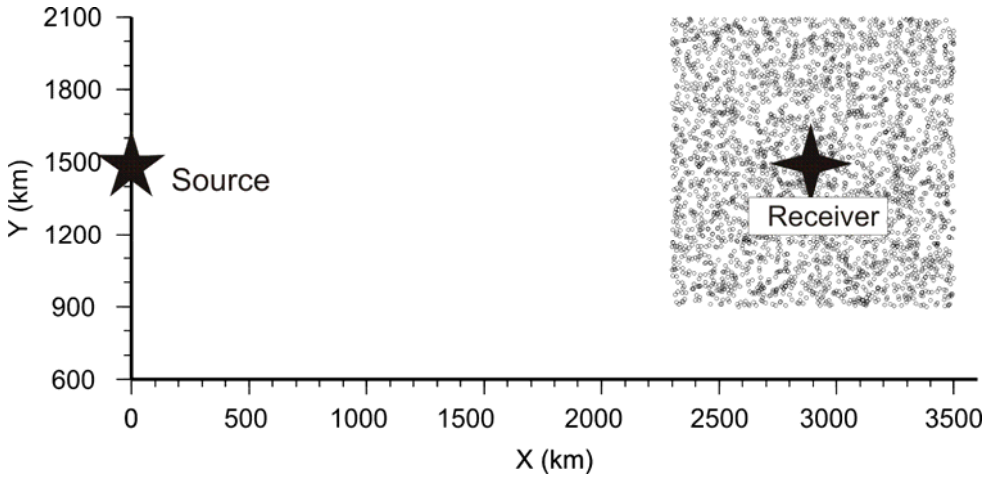

Figure 3-4. Scattering geometry. Scatterer locations within the region centred on the receiver are uniformly and randomly distributed.

To obtain seismic traces at the source-scatterer and scatterer-receiver offset distances appropriate for their use in the numerical convolution (equation 3-4)), I used a τ-p wavefield interpolation algorithm (Yilmaz, 1987) using the precomputed 2-D synthetic seismic sections.

Numerical evaluation of integral (3-4) was performed by using Monte-Carlo sampling in order to avoid spurious coherency that could be caused by spatial aliasing when using a regular integration grid. The 2-D spatial integral uniformly samples surface points on a random grid simulating constant scattering potential for the entire infinite plane (Figure 3-4). Sixty-four realizations of the random grid, each with 2000 points (Figure 3-4), were computed in parallel on the cluster, and the resulting amplitude envelopes were stacked afterwards to produce the final synthetic coda records (Figure 3-5). As above, the synthetic coda generation was implemented by I. Morozov in an IGeoS tool sharing many of its libraries with other codes.

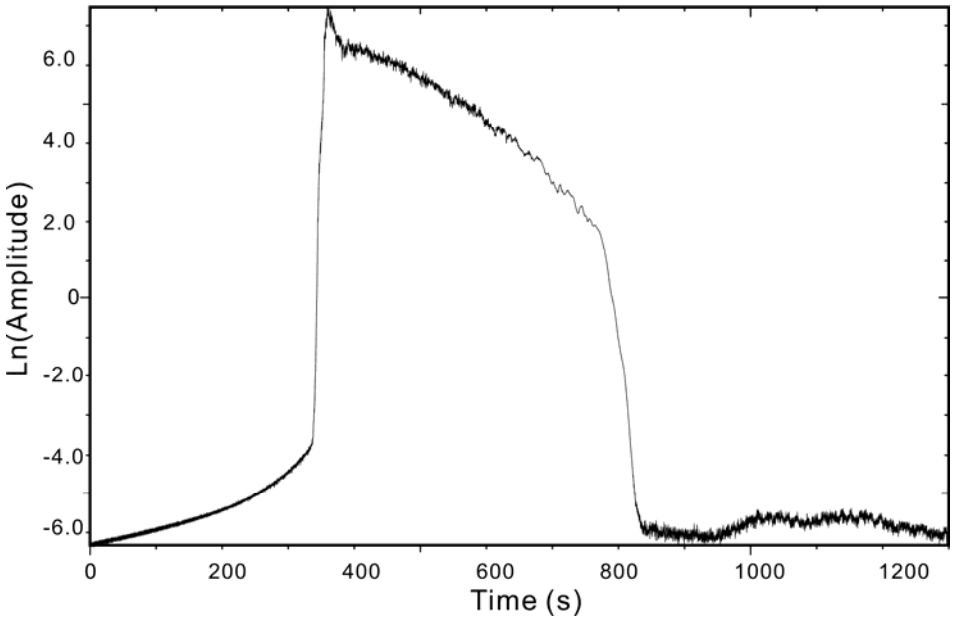

Figure 3-5. Unfiltered natural log(*Amplitude*) synthetic coda in Quartz model (Figure 2a).

4 MODELLING RESULTS AND PNE DATA EXAMPLES

4.1 Coda modeling results

I performed measurements of the synthetic teleseismic *P*-wave codas for each of the four velocity models. Coda traces were band-pass filtered with centre frequencies at 0.4, 0.79, 1.58, 3.16, 4.48, 6.32, 8.94, 12.6, and 17.8 Hz to examine the natural log-amplitude slopes as functions of the frequency (Figure 4-1).

Using the resulting coda records, natural log-amplitude slope measurements were performed on coda envelopes in the manner of Morozov and Smithson (2000) (Figure 4-2). L_2- (RMS) and L_1-norm fitting (e.g., Aster *et al.*, 2002) were tried, with uncertainties

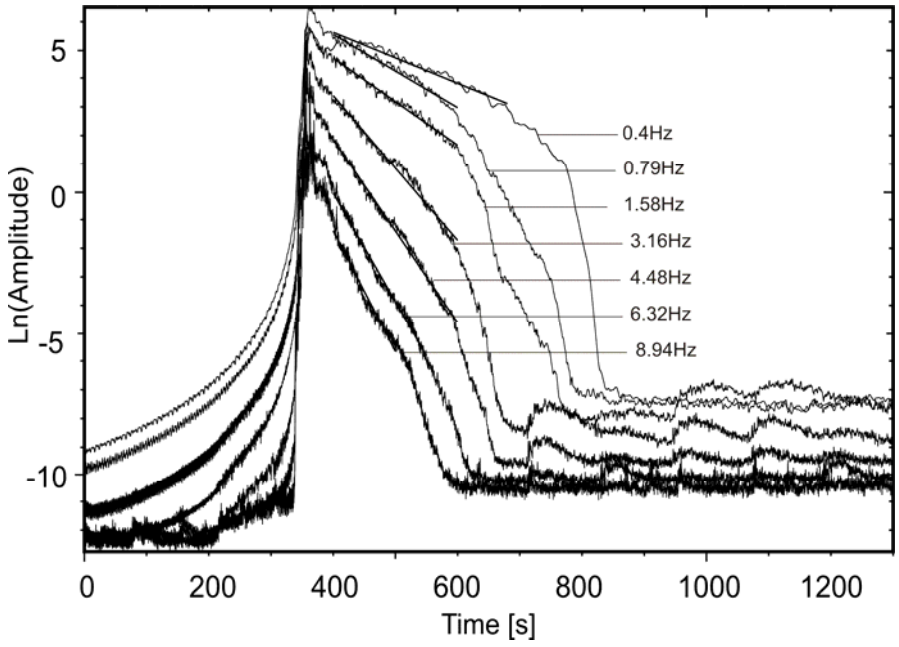

Figure 4-1. Natural log-amplitude synthetic coda for Quartz model (Figure 3-2a, Figure 3-3a, Figure 3-5) at selected frequencies (labelled). Straight lines indicate the measured amplitude fits. Note the progressive change in coda shapes with increasing frequencies.

measured by using 50% jack-knife resampling. Owing to large sampling volumes and stable coda envelopes, the differences between the L_2- and L_1-norm results and the corresponding slope uncertainties were found negligible, and I used L_2 estimates in the subsequent analysis.

Figure 4-2 shows the results for models Quartz and Complex Crust with crustal Q_S = 500. In this Figure, coda slope values show clear linear dependencies on the frequency to about 7-10 Hz, after which the fidelity of modeling appears to drop, and the slopes flatten out (attenuation is replaced by frequency-independent numerical noise of unclear nature). By fitting straight lines to the points within the 0-7 Hz range, I found that the intercepts at f = 0 Hz were non-zero: $\gamma \approx 0.8 \cdot 10^{-2}$ s^{-1} and $\gamma \approx 1.6 \cdot 10^{-2}$ s^{-1} for the two

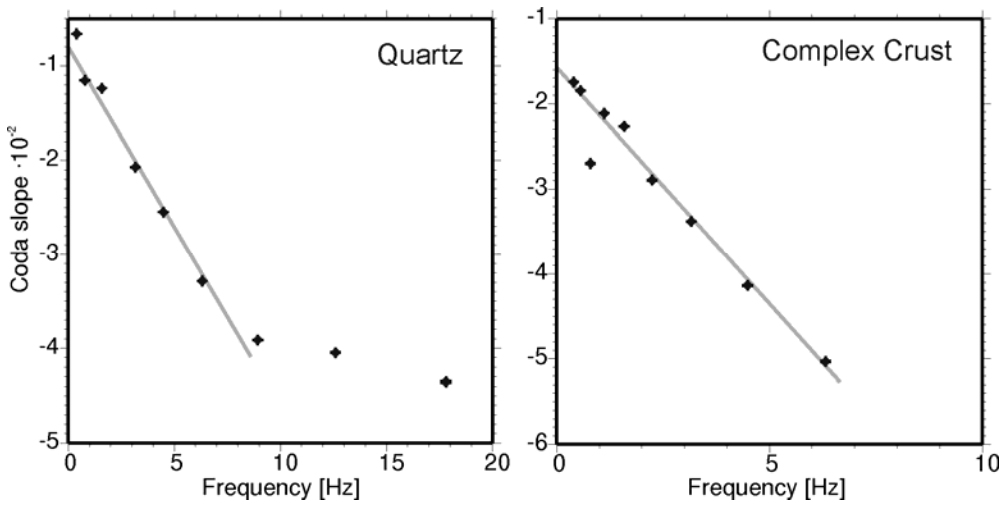

Figure 4-2. Measured natural log-amplitude coda slopes (-b in eq. (2-6)) from models Quartz and Complex Crust with crustal Q_S = 500. Note the linearly decreasing (steepening) coda slopes with frequencies increasing to ~7-10 Hz. Solid grey lines indicate linear regressions using formula (2-10): $\gamma = 0.8 \cdot 10^{-2}$ and Q_e = 800 for Quartz model, and $\gamma = 1.6 \cdot 10^{-2}$ and Q_e = 600 for Complex Crust model.

respective models. From the frequency dependencies of coda slopes, I measured Q_e (equation 2-10), which equalled $Q_e \approx 800$ and 600 in these two respective cases (Figure 4-2). Note that γ turned out to be clearly positive in all cases considered here, indicating that the geometrical attenuation is only partly compensated by the increasing volume of near-surface scattering. Also note the flattening of *slope*(*f*) dependencies at higher frequencies due to the reduction in the signal/noise ratios. The outliers at lower frequencies could likely be related to tuning effects within the crustal layers (Figure 4-2).

In an alternative interpretation, when directly converted to frequency-dependent $Q_{coda}(f)$ by using the conventional equation (2-8), the values of coda amplitude slopes

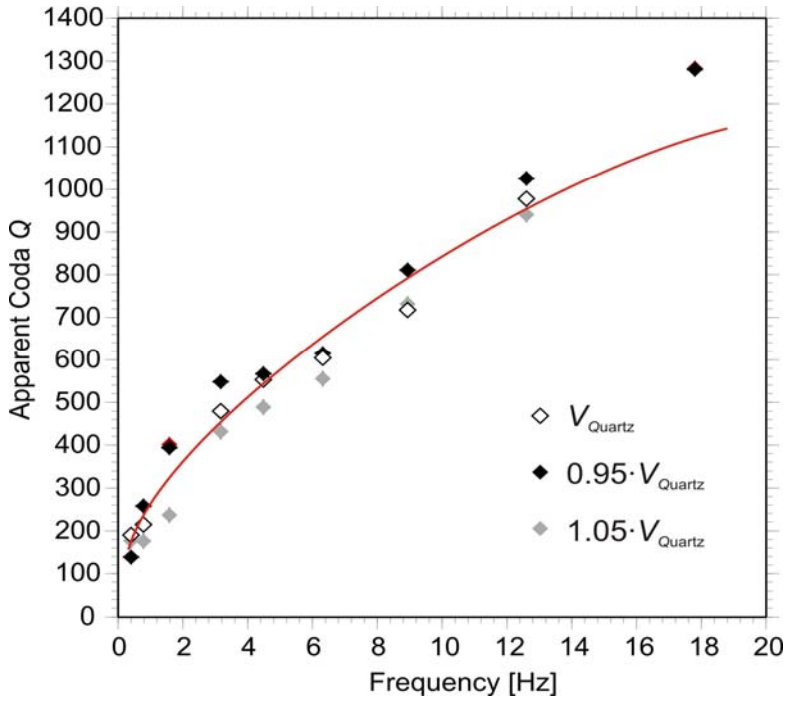

Figure 4-3. Measured natural log-amplitude coda slopes (Figure 4-2) transformed to apparent coda $Q(f)$ determined by relation (2-8). Red line corresponds to $Q(f) = 270\, f^{0.5}$. Note the strong frequency dependence ($\eta \approx 0.5$) of $Q(f)$ despite the constant-Q_S modeled crustal rheology.

could also be fit by using a dependence of type (2-7), with $Q_0 \approx 250$ at 1 Hz and $\eta \approx 0.5$ (Figure 4-3). Although this interpretation could also be acceptable within the data uncertainties, our model contains no rheological or frequency-selective scattering mechanisms to support an *in situ* frequency-dependent attenuation. Therefore the observed coda $Q_{coda}(f)$ (Figure 4-3) should better be viewed as an "apparent" quantity, or as an observational artefact.

By picking linear natural log($A(t)$) dependencies (2-10) for each frequency in the

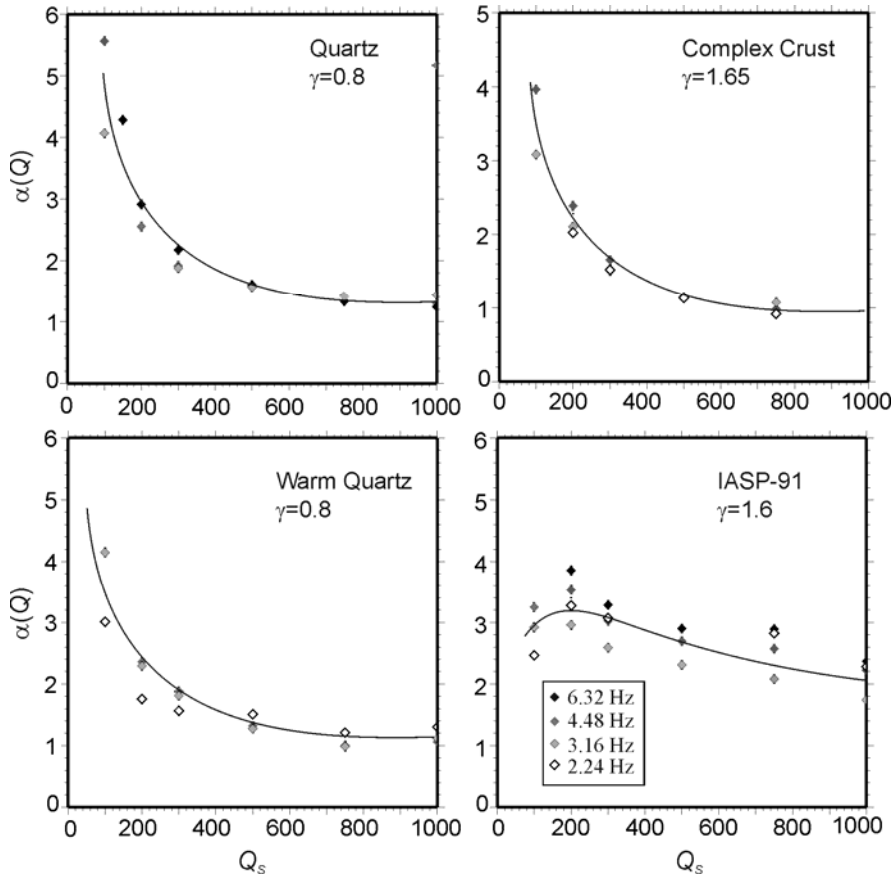

Figure 4-4. $\alpha(Q_S)$ from equation (4-1) for the four models of this study (labelled) and different frequencies (labelled symbols), obtained directly from coda slopes (Figure 4-2) by using the values of γ in equation (2-10) shown in the labels. Lines represent the empirical $\alpha(Q_S)$ dependencies for each velocity structure, picked by hand.

different models, I found that the values of γ stayed approximately constant in most cases that were close to the correct platform structure (values shown in labels in Figure 4-4). By taking advantage of this relative stability of γ's, I attempted empirically relating the observed Q_e to the crustal Q_S. To accomplish this, we transformed the observed coda slopes into Q_e/Q_S ratios:

$$a(Q_s) = \frac{Q_e}{Q_s} = \frac{\pi f}{-Q_s\left(\frac{d \ln A(t, f)}{dt} + \gamma\right)} \tag{4-1}$$

for each frequency (Figure 4-4).

In all models, the resulting $\alpha(Q_S) = Q_e/Q_S$ ratios are nearly frequency-independent, greater than 1, and approach 1 for higher Q_S (Figure 4-4). Because of these properties, frequency-independent curves $\alpha(Q_S)$ can be approximated from numerical modeling in each model, as shown by lines in Figure 4-4. Once such curves are constructed by numerical modeling, they can be utilized for deriving the average crustal Q_S from observations of Q_e.

Interestingly, the $\alpha(Q_S)$ functions are very similar (within ~20% differences) for all three Quartz-based models, despite the strong difference in γ for the Complex Crust model (Figure 4-4). However, the $\alpha(Q_S)$ curve for the IASP91 model (which is definitely inadequate for this area) is strongly different from those for Quartz in its shape, values, and stability in respect to frequency variations (Figure 4-4). Therefore, it appears that with reasonably well-known crustal structures, calibration $\alpha(Q_S)$ curves could be reliably established by numerical modeling.

Finally, both γ and the functional form of $\alpha(Q_S)$ should depend on the structures of the models. I tested this dependence by using four different types of models (3-2) and also by adding velocity perturbations to Quartz model. The results suggest that γ and $\alpha(Q_S)$ indeed correlate with structural model styles and crustal velocities, as will be further discussed in Chapter 5.

4.2 PNE data examples

The use of the (γ, Q_e) model and my numerical simulations allowed us to resolve the following, hitherto puzzling observation from the PNE profiles. Within the East European Platform, measurements from Quartz profile resulted in Q_{coda}(~2 Hz) = 380 and Q_{coda}(~5 Hz) ≈ 430, which was interpreted in the power-law form (2-7) as $Q_{coda}(f) = 270 f^{0.5}$ (Morozov and Smithson, 2000). However, within the Siberian Craton (PNE Kimberlite-3), practically frequency-independent coda amplitude decays were observed, corresponding to $Q_{coda}(f) \approx 1050 f^{1.0}$ (Morozov et al., 2006). Although the intrinsic attenuation was expected to be low within the Siberian Craton, its strong frequency dependence is vastly different from the East European Platform and is surprisingly high even for tectonically active areas (Aki, 1980; Benz et al., 1997; Erickson et al., 2004).

The explanation of the above observations in the (γ, Q_e) form is quite simple. From Quartz-4 data, the natural logarithms of coda amplitudes can be interpreted by using $\gamma \approx 0.75 \cdot 10^{-2}$ s^{-1} and frequency-independent $Q_e \approx 850$, with estimated range of uncertainty of 780 - 960 (Figure 4-5).

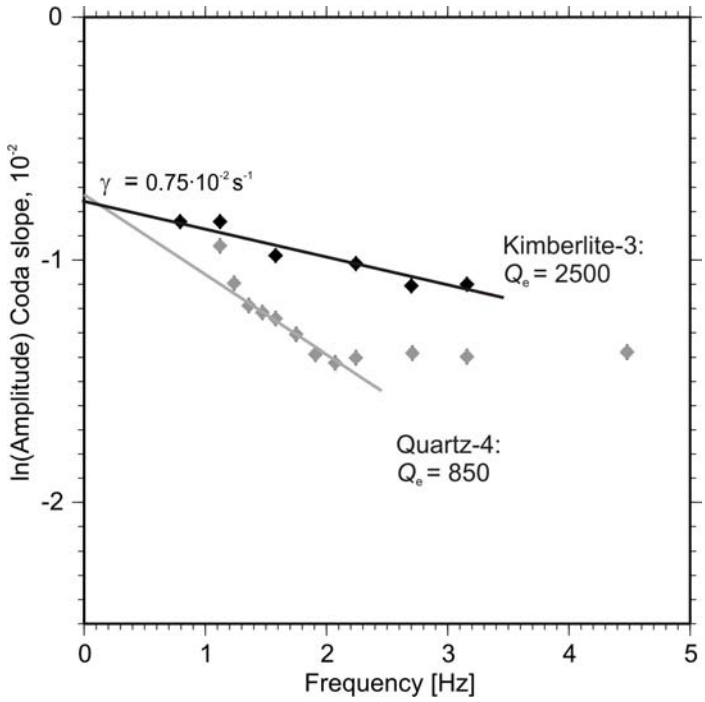

Figure 4-5. Natural log-amplitude coda slopes in real data from PNEs Quartz-4 (recorded within the East-European Platform, at ~2600-km source-receiver offset; same data as in Morozov et al., 2002) and Kimberlite-3 (recording within the Siberian Craton at ~1100-km offsets). Note the different Q_e values (lines and labels), whereas the γ values are similar and close to those modeled (Figure 4-2). Also note that because of lower-magnitude source and longer recording distance, the usable frequency band is narrower for Quartz PNE records.

From Kimberlite-3 records, γ turns out to be nearly the same, but Q_e is much higher: $Q_e \approx 2500 \pm 300$ (Figure 4-5). Note that both values of γ also agree remarkably well with the numerical simulations based on Quartz velocity model data above (Figure 4-2). The high values of Q_e within the Siberian Craton agree with observations of *Pg* waves propagating to over 1600 km from the PNEs (Morozov et al., 2006), for example, as shown in Figure 4-6. These are likely the longest-propagating short-period *Pg* waves observed on Earth (Morozov et al., 2006).

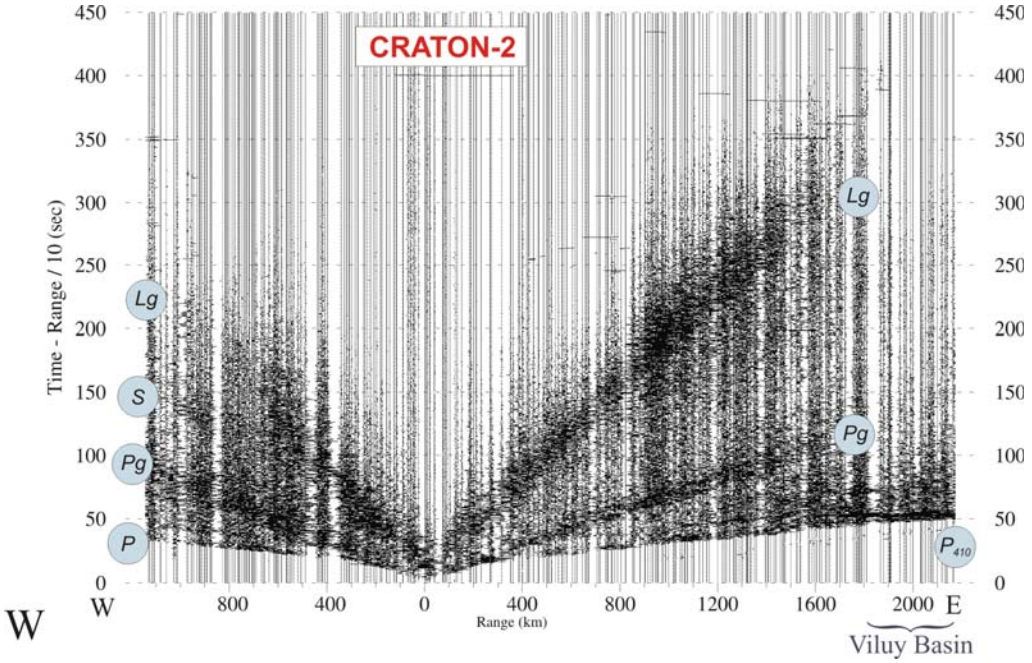

Figure 4-6. Vertical-component record from PNE Craton-2 in Siberian Craton. Regional phases are labelled: *P*, *Pg*, *S*, and *Lg*, and a reflection from the 410-km mantle discontinuity is also indicated (P_{410}). Travel-time reduction velocity of 10 km/s is used. Note the regional phases (*Pg* and *Lg*) traveling to over 1600 km from the source until quickly dissipating within the Viluy Basin. This shows that attenuation within the Siberian Craton is low.

5 DISCUSSION AND CONCLUSIONS

5.1 $\alpha(Q_S)$ and modal content of coda wavefield

In a heterogeneous lithosphere, areas of scattering and attenuation are unevenly distributed and likely are most abundant closer to the surface. Similarly, the seismic wavefield is complex and far from any simple, radial or cylindrical symmetry. Generally, crustal *S* waves should be the primary contributors to the coda, and consequently we expect the observed Q_e to be related to the crustal *S*-wave Q_S. However, the values of Q_S and Q_e may differ. For our model, it appears that because a part of the seismic energy travels through the mantle with typically higher Q_S, we should expect values of Q_e to be greater than the crustal Q_S. In regard to the geometrical attenuation parameter γ in equation (2-10), it could be either negative (corresponding, for example, to strong reflected and diving waves returning additional energy to the surface) or positive, as observed in our modeling. If scattering predominantly occurs near the surface, then values of $\gamma > 0$ should correspond to the scattered energy decaying with distance faster than surface waves, which should be the common case due to: 1) high attenuation of surface waves in the weathered zone (note the Complex Crust model, Figure 4-4), and 2) multiple reflections and scattered seismic waves leaking into the mantle as suggested, for example, by Gupta et al. (1991).

Both γ and the functional form of $\alpha(Q_S)$ depend on the velocity/density structures. A comparison of models Quartz and Complex Crust shows that coda decays are steeper (Figure 4-2) and $\alpha(Q_S)$ values are lower (Figure 4-4) for Complex Crust. Both of these

effects likely result from the presence of the low-Q sedimentary layer in this model. Note that in a detailed study of PNE *Lg Q* in Russia, Li et al. (submitted) pointed out a quantitative correlation of low *Lg Q* with the presence of young (low-velocity) sedimentary basins. From this correlation, a value of $Q_S \approx 60\text{-}70$ was also estimated for these sedimentary rocks.

Notably, in the "realistic" crust/mantle models considered, $\alpha(Q_S)$ is not constant and decreases from ~3-4 at $Q_S = 100$ to about ~1 – 1.4 at $Q_S = 1000$ (Figure 4-4). As expected, the measured values of $\alpha(Q_S)$ are also fairly frequency-independent. By contrast, in the IASP91 model, $\alpha(Q_S)$ is roughly constant within ~2.5 – 3.5 range and somewhat less stable in respect to the frequency variations (Figure 4-4). This means that only in the IASP91 model, the observed Q_e is proportional to Q_S of the crust, and it equals Q_e of Quartz-based models only when $Q_S \approx 100$.

The above observations can be explained by considering two end-member types

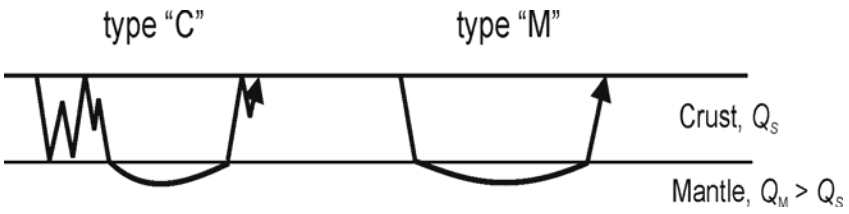

Figure 5-1. Two end-member types of scattered wave paths contributing to the coda. Type C: predominantly crustal propagation with numerous bounces between the crustal boundaries. Type M: paths with at least a proportional contribution from mantle propagation. In all cases, $Q_e > Q_S$; however, modes of type C result in $Q_e \approx Q_S$. Type M leads to increased values of Q_e reaching about $3Q_S$ for the lower values of $Q_S \approx 100$ in our simulations (Figure 4-4).

of waves contributing to the modeled codas (Figure 5-1).

For the first type labelled C, propagation takes place predominantly through the crust, possibly with some contributions from mantle paths (Figure 5-1). For type M, only a fixed portion of the path lies within the crust. With these definitions, I observe that:

1) Waves propagating through the mantle, which generally has higher Q_S values of ~700 – 1000 in our models, increase the observed values of Q_e. This effect is controlled by the relative time seismic waves travel within the mantle, and therefore waves of type M should lead to higher $\alpha(Q_S)$ than those of type C (Figure5-1);

2) Because of its simple crustal structure, the IASP91 model is depleted in crustal waves (diving and converted, Figure 3-3d), and therefore the contribution of mantle scattering paths (type M) in it is significant for any crustal Q_S. For such paths, $\alpha(Q_S)$ is determined by the time seismic waves travel within the crust, which stays approximately constant;

3) Waves of type C are significantly more abundant in the Quartz-based models (Figure 3-3 a-c). With increasing the crustal Q_S, their amplitudes relative to the wave type M should increase, leading to the observed reduced values of $\alpha(Q_S)$. Note that $\alpha(Q_S)$ decreases with increased crustal gradients and reflectivity, and it reaches ≈1 for the Complex Crust model (compare Figures 4-4b to a).

For average crustal $Q_S \leq 100$, seismic waves dissipate quickly, and no significant crustal waves of type C should develop. Therefore, the results from all models should be

similar for such Q_S values. However, note that such low whole-crust Q_S values are still unlikely, and they were not observed in PNE data (Li et al., submitted).

5.2 Coda properties in stable vs. tectonically active regions

Because the (γ, Q_e) parameters appear more directly related to lithospheric properties than (Q_0, η), it would be useful to revisit the observation that active tectonic regions are generally characterized by low Q_0 and high η, and stable cratons – by higher Q_0 and lower η (Aki, 1980; Steensma and Biswas, 1988; Benz et al., 1997; Mandal and Rastogi, 1998; Erickson et al., 2004). By using over 40 worldwide measurements, Morozov (2008a) suggested that the level of $\gamma_d \approx 0.8 \cdot 10^{-2}$ s^{-1} in surface-wave and *Lg Q* measurements separates the tectonically stable ($\gamma < \gamma_d$) from tectonically active ($\gamma > \gamma_d$) zones. Note that both of the PNE coda examples above comply with this criterion. At the same time, the use of quality factors (Q_0 or Q_e) as discrimination criteria could be problematic because these quantities are strongly affected by sedimentary basins (Li et al., submitted) and generally vary quite broadly (Morozov, 2008a).

The reasons for increased γ values within tectonically-active areas still remain to be investigated. In the numerical experiments of this thesis, I tested two possible causes of higher geometrical attenuation: 1) lower-velocity, lower- or inverted-gradient crustal and upper mantle velocity structures, possibly caused by increased crustal temperatures (as in the Warm Quartz model; Christensen and Mooney, 1995), and 2) presence of a low-*Q* layer, as in the Complex Crust model (Figure 3-2). Both Quartz and Complex Crust models were examined with and without the low-*Q* sedimentary layers, and the Quartz model was also tested for ±5% velocity variations within the crust. These testing

results suggested the following observations:

1) Despite what was intuitively expected when the numerical experiments were set up, velocity variations and/or reduced crustal velocity gradients had little effect on the values of γ (Figure 4-3; also compare the results for Quartz and Warm Quartz models in Figure 4-4);

2) A low-Q layer within the upper crust caused γ to increase (compare the Quartz and Complex Crust models; Figure 4-4).

Therefore, a thin, low-Q or scattering layer within the crust most strongly affects the geometrical attenuation, but not Q_e. This surprising at first glance conclusion can be explained by noting that the attenuation effect of a thin layer should be proportional not to the total number of wave cycles (from the source to receiver) but to the number of times the seismic waves traverse it during propagation, which is a geometrical factor. It is likely that a similar effect would be achieved with a low-Q layer located at different depths within the model, or with elastic scattering (e.g., from crustal faults or corrugated Moho) replacing the intrinsic attenuation of the sediments used in our modeling. However, these hypotheses still need to be developed in detailed case and modeling studies, which are outside of the scope of this project.

5.3 $\alpha(Q_S)$ and inversion for attenuation properties of the crust

The stability of γ and $\alpha(Q_S)$ in respect to the variations of crustal Q provides a way for systematic inversion for the average crustal Q_S from (γ,Q_e) measurements First, from the available travel-time data (ideally, from inversion of a refraction/reflection

profile similar to Quartz, travel-time tomography, or Receiver Function studies), a velocity/density model can be constrained. By using numerical modeling in such a structure, γ and the $\alpha(Q_S)$ dependence can be derived as described above. With the help of these functions, bulk crustal Q_S can then be estimated from Q_e observations:

$$Q_S = \frac{Q_e}{\alpha^{-1}(Q_e)}, \tag{5-1}$$

where:

$$Q_e = \frac{\pi f}{-\left(\frac{d \ln A(t, f)}{dt} + \gamma\right)}, \tag{5-2}$$

which should be frequency-independent. In addition, because parameters γ and the *in situ* Q_S in equation (5-1) are related to the crustal structure and not so much to the observations, their use could improve coda magnitude analysis and calibration (Phillips et al., 2004) and coda Q regionalization (Singh and Herrmann, 1983).

The scattering potential Ψ in integral (3-4) was not constrained in my modeling and not critical for the results presented above. However, it was also estimated to match the observed PNE data. Morozov and Smithson (2000) modeled coda power as a function of time by describing the primary event as a parabolic function with peak power P_0 and duration τ, and the relative coda amplitude parameter λ, with the product $\lambda\tau$ giving the power relative to the peak. These authors determined values of $\lambda = 0.22$ for all Quartz events and $\tau = 1.25$ s for the teleseismic P. Applying these values to the synthetic data in this study gives a scattered-amplitude to direct-amplitude ratio of $\sqrt{\lambda\tau} \approx 0.5$. Therefore,

the scattered trace should be approximately half the amplitude (and about ¼ the intensity) of the direct wave at the time of coda onset. From this scaling factor, the scattering potential Ψ per unit area was computed for its use in equation (3-4).

With regard to the validity of the single-scattering coda approximation (eq. 3-4), note that the intensity of the doubly-scattered coda should be approximately ¼ of that of the single-scattered coda considered above. Therefore, we expect that accounting for multiple scattering within the coda could modify the coda intensity by roughly (¼)/(1-1/4) = 1/3. The empirical calibration of the value of Ψ above by using the real PNE data (which is multiply-scattered by nature) should further reduce this error. Therefore, among the other limitations of the present modeling (1D velocity structure, absence of surface topography, only surface scattering, and frequency- and spatially invariant Ψ), the single-scattering model appears to be a reasonable approximation. Moreover, the multiply-scattered coda contributions should likely have similar time-frequency properties, which were the main object of this study.

5.4 Conclusions

Frequency-dependent attenuation is often observed in local, regional, and teleseismic coda measurements, as well as in surface-wave, *Lg*, and borehole studies. Such observations can be interpreted in two ways: via frequency-dependent coda attenuation quality, $Q(f)$, or by means of effective, uncompensated geometrical attenuation (γ, comprising uncompensated geometrical spreading and elastic scattering) and frequency-independent coda attenuation (Q_e). The second of these alternatives offers

a number of major advantages:

1) It is better justified theoretically and does not require unusual crustal rheologies or scale-length selective scattering properties.

2) It can be measured directly and unambiguously from the data, without reliance on compensation of geometrical spreading or other theoretical assumptions.

3) Its parameters can be quantitatively related to the *in situ* lithospheric velocity/density structure (via γ) and attenuation (via Q_e) crustal structures. The resulting Q_e appears to correspond to crustal Q_S and can be directly correlated to the observed *Lg Q*.

4) The stable, frequency-independent parameters allow easier comparisons between different areas and studies around the world. In particular, parameter γ could provide a transportable discriminant for differentiating between the tectonic types and ages of the lithosphere. From a preliminary numerical model, this discriminant may indicate the presence of localized attenuative or scattering structures within the crust.

5) As stable and transportable characteristics, the (γ, Q_e) parameters are likely to improve coda magnitude analysis and coda *Q* regionalization and its correlation with crustal properties.

Numerical modeling of PNE coda wavefields argues strongly in favour of the (γ, Q_e) model and illustrates the mechanisms that could lead to the apparent frequency dependencies of coda $Q(f)$ that are often reported. PNE coda measurements in two different areas in Russia show similar γ values, although with strongly different Q_e.

Wavefield models were proposed to explain the relation of the observed Q_e values to the crustal *S*-wave attenuation quality factors.

Most importantly, the observed values of γ were found to be very close to those derived from completely independent numerical simulations. This correspondence shows the physical consistency of the new attenuation model and illustrates its predictive power.

5.5 Significance of (γ, Q_e) model and suggestions for further research

This study represents only the first application of a new attenuation model to theoretical, computational, and real-data analysis. Although still not sufficiently well recognised, it could open a broad area of possibilities for further research.

Recognition of the spatial variability of the lithospheric attenuation property (γ) could have a major impact on many attenuation studies. Methodologically, this recognition explains and removes the apparent character of $Q(f)$ which makes the interpretations of frequency-dependent Q tricky and uncertain. Most of the existing attenuation results could be reworked in the spirit of the new interpretation. As suggested by Morozov (2008a and 2009), possibly revealing conclusions include widespread frequency-independence of Q_e (within the available data coverage and quality), upward updating of the reported Q values by 20-30 times, discounting the confusing concept of "scattering quality factor" (Q_s), and suggestion of a global depth-band Q model for the Earth replacing the absorption band model (Anderson and Given, 1982). If corroborated by further studies, correlations of regional variations of γ with tectonic structures could provide a solid basis for interpreting geodynamical properties of the lithosphere.

The remarkable success in predicting the attenuation property (γ) by numerical modeling from purely structural information opens new possibilities for linking detailed structural and attenuation studies. Further, detailed studies need to be conducted by using three-dimensional modeling and a more complete coda and other wave models. The Soviet PNE datasets still contain vast volumes of data that can be used in such analysis. In addition, the ~400-station broadband, teleseismic US Array in the United States provides a continuously increasing, well-maintained, high-quality, broad-band, and freely available volume of modern digital data that could be utilized for imaging seismic attenuation and its relation to geologic structures at unprecedented detail.

6 LIST OF REFERENCES

Abercrombie, R. E. (1998). A summary of attenuation measurements from borehole recordings of earthquakes: the 10 Hz transition problem, *Pageoph* **153**, 475-487.

Adams, D. A., and R. E. Abercrombie (1998). Seismic attenuation above 10 Hz in southern California from coda waves recorded in the Cajon pass borehole, *J. Geophys. Res.* **103**, 24,257-24,270.

Aki, K. (1969). Analysis of the seismic coda of local earthquakes as scattered waves. *J. Geophys. Res.* **74**, 615-631.

Aki, K. (1980a). Attenuation of shear-waves in the lithosphere for frequencies from 0.05 to 25 Hz. *Phys. Earth Planet. Inter.* **21**, 50-60.

Aki, K. (1980b). Scattering and attenuation of shear waves in the lithosphere, *J. Geophys. Res*. **85**, 6496-6504.

Aki, K. (1982). Scattering and attenuation. *Bull. Seism. Soc. Am*. **72,** S319-S330.

Aki, K. and B. Chouet (1975). Origin of coda waves: source, attenuation, and scattering effects, *J. Geophys. Res.* **80**, 3,322-3,342.

Aki, K., and Richards, P. G. (2002). Quantitative Seismology, Second Edition, University Science Books, Sausalito, CA.

Anderson, D. L., and J. W. Given (1982). Absorption band Q model for the Earth. *J. Geophys. Res.* **87**, 3,893–3,904.

Aster, R., B. Borchers, and C. Thurber (2002). Parameter Estimation and Inverse Problems, preliminary edition.

Badri, M., and Mooney, H. M., (1987). *Q* measurement from compressional seismic waves in unconsolidated sediments, *Geophysics* **52**, 772-784.

Bannister, S. G., E. S. Husebye, and B. O. Ruud (1990). Teleseismic *P* coda analyzed by three-component and array techniques: deterministic location of topographic *P*-to-*Rg* scattering near the NORESS array, *Bull. Seism. Soc. Am.* **80**, 1969-1986.

Bath, M., (1974). Spectral analysis in geophysics, Elsevier, Amsterdam.

Benz, H., A. Frankel, and D. Boore (1997). Regional *Lg* attenuation in the continental United States, *Bull. Seism. Soc. Am.* **87**, 600–619.

Biswas, N. N. and Aki, K. (1984). Characteristics of coda waves: central and south-central Alaska. *Bull. Seism. Soc. Am.* **74**, 493-507.

Blair, D. P., and Spaths, A. T. (1984). Seismic source influence in pulse attenuation studies, *J. Geophys. Res*. **89**, 9253-9258.

Born, M. and Wolf, E. (1965). Principles of Optics, 3rd edn. Pergamon Press, Oxford.

Brad, P. Y. and Gariel, J. C. (1986). The seismic response of two-dimensional sedimentary deposits with large vertical velocity gradients. *Bull. Seism. Soc. Am.* **76**, 343-366.

Braile, L. (1977). The Earth's crust, AGU Monograph Series, no. 20, *Am. Geophys. Un.*, Washington, DC.

Brzostowski, M. A., and McMechan, G. A., (1992). 3-D tomographic imaging of near-surface seismic velocity and attenuation, *Geophysics* **57**, 396-403.

Campillo, M. (1987). *Lg* wave propagation in a laterally varying crust and the distribution of the apparent quality factor in central France, *J. Geophys. Res.* **92**, 12604-12614.

Campillo, M. (1990). Propagation and attenuation characteristics of the crustal phase *Lg*, *Pageoph* **132**, 1-17.

Canas, J. A., Egozcue, J. J., and Pujadas, L. (1988). Seismic attenuation in southern Mexico using the coda Q method. *Bull. Seism. Soc. Am*. **78**, 1807-181.

Carpenter, P. I., and Stanford, A. R., (1985). Apparent *Q* for upper crustal rocks of the central Rio Grande Rift, *J. Geophys. Res*. **90**: 8661-8674.

Christensen, N. I., and W. D. Mooney (1995). Seismic velocity structure and composition of the continental crust: A global view, *J. Geophys. Res.* **100**, B7, 9761-9788.

Chubak, G., and I. B. Morozov (2006). Integrated software framework for processing of

geophysical data, *Computers & Geosciences* **32**, 767-775.

Cleary, J. R. and Haddon, R. A. W. (1972). Seismic wave scattering near the core-mantle boundary: Anew interpretation of precursors to PKIKP, *Nature*, **240**, 549-550.

Dainty, A. M. (1981). A scattering model to explain seismic Q observations in the lithosphere between 1 and 30 Hz, *Geophys. Res. Lett.* **8**, 1126-1128.

Dainty, A. M. (1985). Air Force Geophysical Laboratory Report, AFGL-TF-86-0218.

Dainty, A. M. (1990). Studies of coda using array and three-component processing, *Pageoph* **132**, 221-244.

Dainty, A. M. and C. A. Schultz (1995). Crustal reflections and the nature of regional *P* coda, *Bull. Seism. Soc. Am.* **85**, 851-858.

Dainty, A. M. and Toksoz, M. N. (1981). Seismic codas on the Earth and the Moon: a comparison. *Phys. Earth Plant. Inter.* **26**, 250-260.

Del Pezzo, E., Ferulano, F., Giarrusso, A. and Martini, M. (1983). Seismic coda, Q and scaling law of the source spectra at the Aeolian Islands, southern Italy. *Bull. Seism. Sac. Am.* **73**, 97-108.

Der, Z. A., A. C. Lees, and V. F. Cormier (1986). Frequency dependence of *Q* in the mantle underlying the shield region of Eurasia, Part III: The *Q*-model, *Geophys. J. R. Astr. Soc.* **87**, 1103-1112.

Enderle, U., M. Titgemeyer, M. Itzin, C. Prodehl, and K. Fuchs (1997). Scales of structure in the lithosphere - Images of processes, *Tectonophysics* **275**, 165-198.

Erickson, D., D. E. McNamara, and H. Benz (2004). Frequency-dependent *Lg Q* within the continental United States, *Bull. Seism. Soc. Am*. **94**, 1630–1643.

Espinosa, A. F. (1968). Ground amplification studies of short-period seismic waves, In Studies in Seismicity and Earthquake Damage Statistics, Part I; Report for Housing and Urban Development agency (HUD), ESSA Technical Report, Coast and Geodetic Survey, 1-12.

Espinosa, A. F. (1969). Ground amplification of short-period seismic waves at two sites

neai" Bakersfield. California. *Earthquake Notes* **40**, 3-20.

Espinosa, A. F. (1971). Ground surface motion synthesis and theoretical amplification effects due to shear waves labs.I, General Assembly IASPEI, Symposium on Forerunners of Strong Earthquakes, Moscow, *SSSR* **3**, 34 (I-5), and *Acad. Sci. Comptes Rendus* **17**, 128.

Espinosa, A. F. and Algermissen, S. T. (1972a). Soil amplification studies in areas damaged by the Caracas earthquake of July 29, 1967. *Proceedings of the International Conference on Microzonation* **I I**, 455-464.

Espinosa, A. F. and Algermissen, S. T. (1972b). Study of soil amplification factors in earthquake damaged areas: Caracas, Venezuela. *National Oceanic and Atmospheric Administration, Technical Report* ERL280-ESL 31,201 pp.

Ewing, W. M., Jardentzky, W. S. and PRESS, F. (1957). Elastic Waves in Layered Media, McGraw-Hill, New York.

Frankel, A., A. McGarr, J. Bicknell, J. Mori, L. Seeber, and E. Cranswick (1990). Attenuation of high-frequency shear waves in the crust: measurements from New York state, South Africa, and southern California, *J. Geophys. Res*. **95**, 17441-17457.

Fuchs, K., and G. Müller (1971). Computation of synthetic seismograms with the reflectivity method and comparison with observations, *J. R. Astronom. Soc*. **23**, 417-433.

G-Akis Tselentis (1998). Intrinsic and Scattering Seismic Attenuation in W. Greece, *Pure Appl. Geophys.* **153,** 703-712.

Gao, L. S. (1984). Coda waves analysis for distinguishing attenuation due to isotropic scattering from attenuation due to absorption. *Pure Appl. Geophys.* **122,** 1-9.

Gao, S., (1997). A Bayesian non-linear inversion of seismic body-wave attenuation factors, *Bull. Seism. Soc. Am*. **87**, 961-970.

Geist, A., Beguelin, A, Dongarra, J., Jiang, W, Manchek, R.and Sunderam, V. (1994a). PVM 3 Users Guide and Reference Manual. Oak Ridge National Laboratory, Oak

Ridge, TN.

Geist, A., Beguelin, A., Dongarra, J., Jiang, W., Manchek, R.and Sunderam, V. (1994b). PVM: Parallel Virtual Machine, A users guide and tutorial for networked parallel computing: The MIT Press, Cambridge, Massachusetts.

Geist, A., Kohl, J. A., and Papadopoulos, P. M. (1996). PVM and MPI: A comparison of features. *Calculateurs Paralleles* **8(2).**

Gladwin, M. T., and Stacey, F. D., (1974). Anelastic degradation of acoustic pulses in rock, *Phys. Earth Planet. Inter.* **8**, 332-336.

Gorich, M., and Muller, G. (1987). Apparent and intrinsic *Q*, the one-dimensional case, *J. Geophys.* **61,** 46-54.

Grad, M., and Luosto, U., (1994). Seismic velocities and Q-factors in the uppermost crust beneath the SVEKA profile in Finland, *Tectonophysic* **230**, 1-18.

Greenfield, R. J. (1971). Short-period *P*-wave generation by Rayleigh-wave scattering at Novaya Zemlya, *J. Geophys. Res.* **76**, 7988-8002.

Gupta, I.N., T. W. McElfresh, and R. A. Wagner (1991). Near-source scattering of Rayleigh to *P* in teleseismic arrivals from Pahute Mesa (NTS shots, in: Taylor, S. R., H. J. Patton, and P. G. Richards (Eds.), Explosion Source Phenomenology, *AGU Geophys. Monograph* **65**, 151 - 160.

Gusev, A. and Lemzikov, V. K. (1985). Properties of scattered elastic waves in the lithosphere ofKamchatka: Parameters and temporal variations. *Tectonophysics* **112,** 137-153.

Haddon, R. A. W. (1972). Corrugations on the mantle-core boundary or transitions layers between inner and outer cores? EOS Transactions AGU **53**, 600.

Halderman, T. P., and Davis, P. M., (1991). Q_p beneath the Rio Grande and East African Rift zones, *J. Geophys. Res*. **96**: 10113-10128.

Hasegawa, H. S. (1985). Attenuation of L_g waves in the Canadian Shield, *Bull. Seism. Soc. Am*. **75**, 1569-1582.

Herraiz, M. and Espinosa, A.F. (1987). Coda waves: a review, *Pageoph* **125**, 499-577.

Herramann, R. B. (1980). Q estimates using the coda of local earthquakes. *Bull. Seism. Soc, Am.* **70,** 447-468.

Jannsen, D., Voss, J., and Theilen, F. (1985). Comparison of methods to determine *Q* in shallow marine sediments from vertical reflection seismograms, *Geophys. Prospect.* **33**, 479-497.

Jeffres, H. (I959). The Earth, its origin, history and physieal constitution, Cambridge University Press, **4th** edition.

Jin, A. and Aki, K.(1986). Temporal change in coda Q before the Tangshan earthquake of 1976 and the Haicheng earthquake of 1975. *J. Geophys. Res.* **91**, 665-673.

Kennett, B. L. N. and R. Engdahl (1991). Traveltimes for global earthquake location and phase identification, *Geophys. J. Int.* **105**, 429-465.

Kinoshita, S. (1994). Frequency-dependent attenuation of shear waves in the crust of the southern Kanto area, Japan, *Bull. Seism. Soc. Am*. **84**, 1387-1396.

Lee, W. H. K., Aki, K., Chouet, B., Johnson, P., Marks, S., Newberry, J. T., Rrall, A. S., Stewart, S. W. and Tottingham, D. M. (1986). A preliminary study of coda Q in California and Nevada. *Bull. Seism. Soc. Am*. **76**, 1143-1150.

Levin, F. K. and Robtnson, D. J. (1969). Scattering by a random field of surface scatterers. *Geophysics,* **34,**170-179.

Li, H., I. B. Morozov, and S. B. Smithson (submitted to *Bull. Seism. Soc. Am.*) Mapping *Lg* Q at 1-3 Hz in Northern Eurasia using nuclear-explosion profiles, manuscript available from: http://seisweb.usask.ca/downloads/Papers/LGQ/ .

Liu, H. P., Anderson, D. L., Kanamori, H. (1976). Velocity dispersion due to inelasticity: implications for seismology and mantle composition, *Geophys. J. R. Astr. Soc.* **47**, 41–58.

Mandal, P., and Rastogi, B. K. (1998). A frequency-dependent relation of coda *Qe* for Koyna-Warna region, India, *Pageoph* **153,** 163-177.

Marion, D. P., and Coudin, P.(1992). From ray to effective medium theories in stratified media: an experimental study: Ann. Internat. Mtg., *Soc. Expl. Geophys.,* Expanded Abstracts, 1341–1243.

Matheney, M. P., and Nowack, R. L., (1995). Seismic attenuation values obtained from instantaneous frequency matching and spectral ratios, *Geophys. J. Int*. **123**, 1-15.

Matheney, M. P., Nowack, R. L., and Tréhu, A. M., (1997). Seismic attribute inversion for velocity and attenuation structure using data from the GLIMPCE Lake Superior experiment, *J. Geophys. Res.* **102**, 9949-9960.

Mayeda, K., and W. R. Walter (1996). Moment, energy, stress drop, and source spectra of western United States earthquakes from regional coda envelopes, *J. Geophys. Res*. **101**, 11195-11208.

McNamara, D. E. (2000). Frequency-dependent *Lg* attenuation in south-central Alaska, *Geophys. Res. Lett*. **27**, 3949–3952.

McNamara, D. E., T. J. Owens, and W. R. Walter (1996). Propagation characteristics of *Lg* across the Tibetian Plateau, *Bull. Seism. Soc. Am*. **86**, 457-469.

Mechie, J., A. V. Egorkin, K. Fuchs, T. Ryberg, L. Solodilov, and F. Wenzel (1993). *P*-wave velocity structure beneath northern Eurasia from long-range recordings along the profile Quartz, *Phys. Earth Planet. Inter*. **79**, 269-286.

Mitchell, B. J. and L. Cong (1998). *Lg* coda *Q* and its relation to the structure and evolution of continents: a global Perspective, *Pegeoph*. **153,** 655–663.

Mitchell, B. J., Pan, Y., Xie, J., Cong, L. (1997). *Lg* coda *Q* variation across Eurasia and its relation to crustal evolution, *J. Geophys. Res*. **102,** 22767–22779.

Morasca, P., Mayeda, K., Gök, R., Phillips, W. S., and Malagnini, L. (2008). 2D Coda and Direct-Wave Attenuation Tomography in Northern Italy, *Bull. Seism. Soc. Am*. **98**, 1936–1946.

Morozov, I, B. (2008). Frequency Dependence of Coda Q, Part I: Numerical Modeling and Examples from Peaceful Nuclear Explosions, *Bull. Seism. Soc. Am*. **98**, 2615-2628.

Morozov, I, B. (submitted to GJI) Variability of geometrical spreading as the cause of $Q(f)$ dependence and spurious scattering Q_s.

Morozov, I. B. (2001). Comment on "High-frequency wave propagation in the uppermost mantle" by T. Ryberg and F. Wenzel, *J. Geophys. Res.* **106**, 30,715-30,718.

Morozov, I. B. (2008a). Geometrical attenuation, frequency dependence of *Q*, and the absorption band problem, *Geophys. J. Int*. **175**, 239-252.

Morozov, I. B. (2008b). Open-source software framework integrates data analysis, EOS, Trans. *Am. Geophys. Union* **89**, 261-262.

Morozov, I. B. (2009). Thirty years of confusion around "scattering *Q*"?, *Seism. Res. Lett.* **80** (1), 5-7.

Morozov, I. B., and S. B. Smithson (2000). Coda of long-range arrivals from nuclear explosions, *Bull. Seism. Soc. Am.* **90**, 929-939.

Morozov, I. B., E. A. Morozova, and S. B. Smithson (1998a). On the nature of the teleseismic *Pn* phase observed in the recordings from the ultra-long profile "Quartz", Russia, *Bull. Seism. Soc. Am.* **88**, 62-73.

Morozov, I. B., E. A. Morozova, S. B. Smithson, and L. N. Solodilov (1998b). 2-D image of seismic attenuation beneath the Deep Seismic Sounding profile "Quartz", Russia, *Pageoph* **153**, 311-348.

Morozov, I., Morozova, E., Zhang, C. Chubak, G., Phillips, W.S. and Lipovetsky, I. (2006). Magnitude-yield and travel-time calibration of northern Eurasia using deep seismic sounding datasets, 28-th NNSA/DOE Seismic Research Review, Orlando, FL, September 2006.

Morozov, I., Morozova, E., Zhang, J. Duenow, E. A. Morozov, and S. B. Smithson (2008). Frequency dependence of coda Q: Part I. Numerical modeling and examples from Peaceful Nuclear Explosions, *Bull. Seism. Soc. Am.* **98 (6)**, 2615-

2628.

Morozova, E. A., I. B. Morozov, S. B. Smithson., and L. N. Solodilov (1999). Heterogeneity of the uppermost mantle beneath Russian Eurasia from the ultra-long range profile QUARTZ, *J. Geophys. Res*. **104** (B9), 20,329-20,348.

Nakamura, Y., Latham, G. V., Ewing, M. and Dorman, J. (1970). Lunar seismic energy transmissions[abs.]. *LOS Transactions AGU* **5I**, 776.

Nikolayev, A. V. (1968). Seismic properties of weakly heterogeneous media (English Trans.). *Izv. Akad.Nauk SSSR, Fiz. Zemli* **2,** 83-87.

Nikolayev, A. V. and Tregub, F. S. (1970). A statistical model of the earth crust: Method and results. *Tectonophysics* **10**, 573-578.

Nordyke, M.D. (2000). The Soviet Program for Peaceful Uses of Nuclear Explosions, U. S. Department of Energy, University of California Lawrence Livermore National Laboratory.

Novelo-Casanova, D. A. and Butler, R. (1986). High frequency seismic coda and scattering in the northwest Pacific. *Bull. Seism. Soc. Am.* **76**, 617-626.

Nuttli, O. W. (1973). Seismic wave attenuation and magnitude relations for eastern North America, *J. Geophys. Res.* **78**, 5212-5218.

Padhy, S. (2005). A scattering model for seismic attenuation and its global application, *Phys. Earth Planet. Inter*. **148**, 1-12.

Patanjali Kumar, C. H., Sarma, C. S. P., Shekar, M., and Chadha, R. K. (2007). Attenuation studies based on local earthquake Coda waves in the southern Indian peninsular shield, *Natural Hazards* **40**, 527-536.

Pavlenkova, G. A., Priestley, K., and Cipar, J. (2002). 2D model of the crust and uppermost mantle along rift profile, Siberian craton. *Tectonophysics* **355**, 171-186.

Peterson, J.A. and Clarke, J.W. (1991). Geology and Hydrocarbon Habitat of the West Siberian Basin, 32. *American Association of Petroleum Geologists*, Tulsa, Oklahoma, 93 pp.

Phillips, W. S. and Aki, K. (1986). Site amplification of coda waves .from local earthquakes in central California. *Bull. Seism. Soc. Am*. **76,** 627-648.

Phillips, W.S, Lee, W.H.K. and Newberry, J.T.(1988). Spatial variation of crustal codaQ in California, *Pure Appl. Geophys.* **128**, 251-260.

Phillips, W.S., Patton, H.J. Taylor, S.R. Hartse, H.E. and Randall, R. E. (2004). Calibration for coda based magnitude and yield, *26th Seismic Research Review* 449-456, Orlando, Florida.

Pilant, W. (1979). Elastic Waves in the Earth, Developments in Solid Earth Geophysics, **11**, Elsevier, Amsterdam, 506pp.

Pulli, J. J. (1984). Attenuation of coda waves in New England. *Bull. Seism. Soc. Am.* **74,** 1149-1166.

Rautlan, T. G., Khalturin, V. I., Martinov, V. G. and Molnar, P. (1978). Preliminary analysis of thespectral content of P and S waves from local earthquakes in the Garm, Tadjikistan region. *Bull. Seism. Soc. Am*. **68**, 949-971.

Rebollar, C.J., Traslosheros, C., and Alvarez, R.(1985). Estimates of seismic wave attenuation in northern Baja California. *Bull. Seism. Soc. Am*. **75**, 1371-1382.

Roecker, S. W., Tucker, B., King, J. and Hatzfeld, D. (1982). Estimates of Q in central Asia as a function of frequency and depth using the coda of locally recorded earthquakes. *Bull. Seism. Soc. Am*. **72**, 129-149.

Rosen, O.M. (2003). The Siberian craton: tectonic zonation and stages of evolution. *Geotectonics* **37**, 175–192.

Rosen, O.M., Condie, K.C., Natapov, L.M., and Nozhkin, A.D. (1994). Archean and Early Proterozoic evolution of the Siberian Craton: a preliminary assessment, Archean Crustal Evolution, Amsterdam, Elsevier, 411–459.

Rovelli, A. (1982). On the .frequency dependence of Q in Friuli from short-period digital records. *Bull. Seism. Soc. Am*. **72,** 2369-2372.

Ryberg, T., and F. Wenzel (1999). High-frequency wave propagation in the uppermost

mantle, *J. Geophys. Res.* **104**, 10,655-10,666.

Ryberg, T., K. Fuchs, A. V. Egorkin, and L. Solodilov (1995). Observations of high-frequency teleseismic Pn on the long-range Quartz profile across northern Eurasia, *J. Geophys. Res*. **100**, 18151-18163.

Şahin, S.(2008). Lateral variations of coda Q and attenuation of seismic waves in Southwest Anatolia, *Journal of Seismology* **12**, 367-376.

Sato, H. (1986). Temporal change in attenuation intensity before and after the eastern Yamanashi earthquake of 1983, in central Japan, *J. Geophys. Res.* **91**, 2049-2061.

Sato, H. (1988). Temporal change in scattering and attenuation associated with the earthquake occurrence: A review of recent studies on coda waves, *Pure Appl. Geophys.* **126,** 465-497.

Sato, H. (1990). Unified approach to amplitude attenuation and coda excitation in the randomly inhomogeneous lithosphere, *Pageoph* **132**, 1-29.

Sato, H., and M. Fehler (1998). Seismic Wave Propagation and Scattering in the Heterogeneous Earth, Springer-Verlag, New York.

Saunders, A.D., England, R.W., Reichow, M.K. and White, R.V. (2005). A mantle plume origin for the Siberian Traps: uplift and extension in the West Siberian Basin, Russia. *Lithos* **79**, 407-424.

Savage, J. (1966). Thermoelastic attenuation of elastic waves by cracks. *J. Geophys. Res*. **71,** 3929-3938.

Scherbaum, F. and Kisslinger, C. (1985). Coda *Q* in the Adak seismic zone. *Bull. Seism. Soc. Am.* **75**, 615-620.

Shapira, A.(1989). Coda *Q* estimate in Southern Africa. *Bull. Seism. Soc. Am*. **79**, 914-916.

Singh, S., and R. B. Herrmann (1983). Regionalization of crustal coda *Q* in the

Continental United States, *J. Geophys. Res*. **88**, 527-538.

Steensma, G. J., and Biswas, N. N. (1988). Frequency Dependent Characteristics of Coda Wave Quality Factor in Central and South-central Alaska, *Pageoph* **128**, 295-307.

Sultanov E *et al.* (1999). Ecological monitoring with the public's participation at sites noted for high biodiversity and vulnerability of ecosystems along Baku-Supsa oil pipeline. *Baku-Tbilisi.* 124 pp.

Takano, K. (1971). Analysis of seismic coda of ultra-microearthquakes in the Matsushiro area, A comparison with Parkfield, California. *J. Phys. Earth* **19***,* 209-216.

Taner, M.T., Koehler, F., and Sheriff, R. E. (1979). Complex seismic trace analysis, *Geophysics* **44**, 1041-1063.

Tonn, R. (1989). Comparison of seven methods for the computation of *Q*, *Phys. Earth Planet. Inter.* **55**, 259-268.

Warren, N. (1972). *Q* and structure, *Earth, Moon, and Planets*, **4 (3-4)**, 430–441, Springer, Netherlands.

Wesley, M. P. (1965). Diffusion of seismic energy in the near range. *J. Geophys. Res.* **70,** 5099-5106.

Wessel P., and W. H. F. Smith (1995). New version of the Generic Mapping Tools released, EOS, *Trans. Am. Geophys. Union* **76**, 329.

White, R. E. (1992). The accuracy of estimating *Q* from seismic data, *Geophysics* **57,** 1506-1511.

Wong,V., Rebollar, C. J. and Munguía, L. (2001). Attenuation of Coda Waves at the Tres Virgenes Volcanic Area, Baja California Sur, Mexico. *Bull. Seism. Soc. Am.* **91,** 683-693.

Woodgold, C. R. D.(1990). Estimation of Q in Eastern Canada using dcoda waves. *Bull. Seism. Soc. Am.* **80,** 4ll-429.

Wright, C. and Hoy, D. (1981). A note on pulse broadening and anelastic attenuation in

near-surface rocks, *Phys. Earth Planet. Inter.* **25**: P1-P8.

Wu, R.-S., (1985). Multiple scattering and energy transfer of seismic waves, separation of scattering effect from intrinsic attenuation, *Geophys. J. R. Astr. Soc.* **82**, 57-80.

Yilmaz, O. (1987). Seismic Data Processing. SEG.

Yun, Sukyoung, Lee, Won Sang, Lee, Kiehwa, and Noh, Myung Hyun (2007). Spatial Distribution of Coda Q in South Korea. *Bull. Seism. Soc. Am.* **97,** 1012-1018.

Zelt, B. C. Dotzev, N. T. Ellis, R. M. and Rogers, G. C.(1999). Coda Q in Southwestern British Columbia, Canada. *Bull. Seism. Soc. Am.* **89,** 1083-1093.

Zener, C. M, (1948). Elasticity and Anelasticity of Metals, University of Chicago Press, Chicago.

Zonenshain, L.P., Kuzmin, M. I., and Natapov, L.M. (1990). Geology of the USSR: A Plate Tectonic Synthesis, *Geodyn. Ser.* **21**, AGU, Washington, D.C.

7 APPENDICES

7.1 APPENDIX A: IGeoS data processing flow and computing time test

7.1.1 IGeoS processing flow for synthetic coda generation and modeling

All my numerical modeling tests were implemented by using IGeoS software package under the Parallel Virtual Machine parallelization system (PVM; e.g., Geist, et al., 1994a, 1994b, 1996). PVM is a software that permits a heterogeneous collection of Unix and/or Windows computers to interact by exchanging data and commands and act as a single, large parallel computer. By working under PVM, the programmer can follow the same process of 'sharing and passing information' between different processors and user interfaces.

The simplified flow chart of this procedure is shown in Figure 3-6, in which a Green's function modeling process is used as an example. Generally, the 'master' process collects information and commands from user interface (which actually may be some job or shell scripts under IGeoS), performs initial processing of this information, and then assigns computationally-intensive parts of the modeling task to each processor (Figure A-1). The processors work on their tasks independently and concurrently by using the information sent by the master. Once they finish their tasks, they pass their results and output data to the master. The master collects all the necessary data from each processor and combines them in a common dataset again. Finally, once all slave processes finish

their tasks, the master process performs the remaining part of processing and sends the results to the output.

I used a 66-processor 1.6-GHz AMD Opteron cluster with additional 2-processor master and input/output nodes, and therefore the largest number of parallel slave

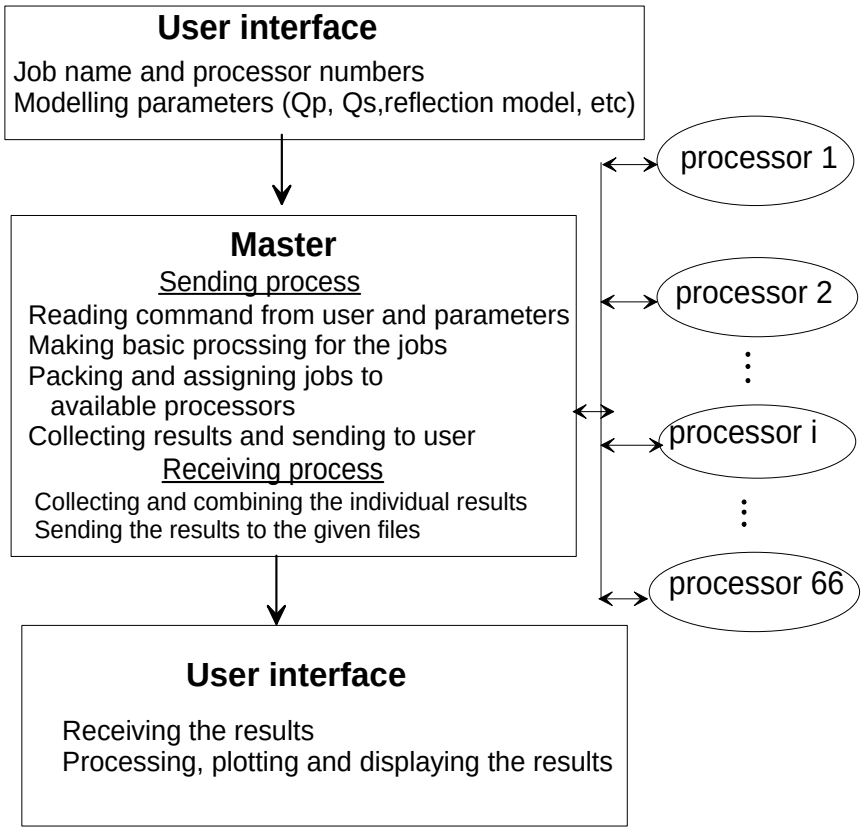

Figure A-1. Structure of IGeoS processing flow under PVM, represented by numerical modeling processing flows.

processes used was 66. The synthetic coda modeling process followed a similar procedure.

7.1.2 Computing time test

With all 66 processors available to the same IGeoS processing flow, the modeling computing time required for computing the Green's function in, for example, Quartz model, was about 9 ½ hours. It is a reasonable computing time for such complex modeling. The parallelization approach implemented in my study was based on the fact that 1-D waveform modeling was performed in the frequency domain (Fuchs and Muller, 1975), and therefore different frequency sub-bands could be distributed among the processors. When modeling was completed for each frequency band, the resulting time-domain records were stacked to produce the full-band data This approach contained little inter-process communication and therefore provided high computing efficiency, and it worked well through all my modeling jobs. However, in order to measure the efficiency of such code parallelization under PVM, I conducted a code speed-up test by using smaller subsets of the available 66 processors. The synthetic model "Quartz" was used as the example.

When a single processor was used, it took 380.18 hours for one modeling, while when all 66 processors are involved to compute, it only took 9.33 hours. I tested performance when the modeling job with the numbers of slave processors equal 5, 10, 15 .. 60, at increments of 5 processors (Figure A-2). For easier interpretation of the results, I plot in Figure A-2 the speed-up factor resulting from using *n* processors as compared to a single-processor computation:

$$F(n) = \frac{T(1)}{T(n)}, \qquad \text{(A-1)}$$

where $T(n)$ is the total ("wall clock") computation time by using n slave compute processes. This time was reported by IGeoS tool `info` when the modeling was completed.

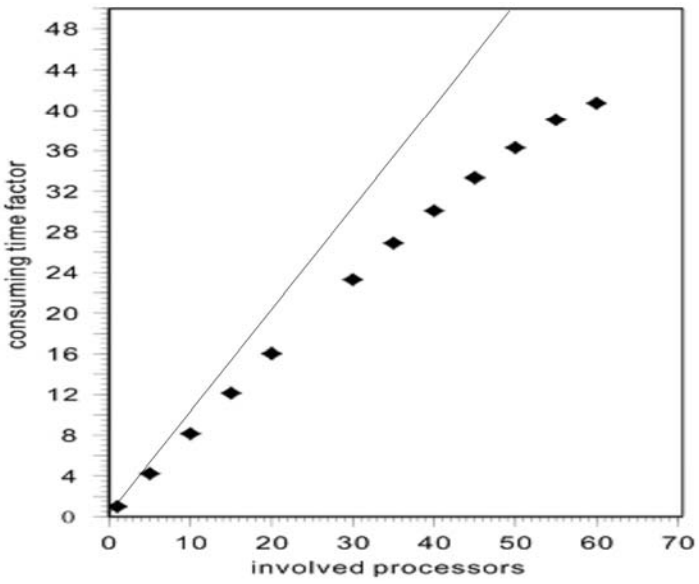

Figure A-2. Speed up parameter $F(n)$ as a function of the number n of the processors involved in Green's function modeling in model Quartz (Figure 3-3). Straight line corresponds to F(n) = n

With no overhead from PVM network communications and disk input/output, this speed-up factor should equal $F(n) = n$, As Figure A-2 shows, $F(n)$ is indeed approximately linear with n and somewhat below this level to about $n \approx 40$, after which the speed-up becomes less efficient. This was expected, because the wavenumber summation (Fuchs and Muller, 1975) involves little network traffic apart from the initial set up and closing downloading of the results. The principal limitation was only in the computational load on the processors. From this test, I concluded that the utilization of the cluster was sufficient and well justified, and the code was efficiently parallelized.

7.2 APPENDIX B: Worldwide summary of coda *Q*

In the table below, the meanings of Q_0 and η are detailed in eq.(2-9); Most Q_{coda} values in fourth column are given directly by these authors, and some of them are transformed from the coda pictures given by the authors. In some areas, the *Q* values are various for the same frequency band, which shown as a value range here. The single frequency value in the "frequency band" column stands for central frequencies with frequency band-pass filter.

Table B-1 Summary of worldwide studies of coda *Q*

Region	Q_0 and η	Frequency (band) (Hz)	Q_{coda}	Active *vs* stable	References
Tsukuba, Kanto (area T), Japan	200; 1	1.5	280	active	Aki and Chouet (1975)
		3	400		
		6	500		
		12	1000		
		24	1800		
Stone Canyon California	70; 1	1.5	90	active	Aki and Chouet (1975)
		3	130		
		6	240		
		12	500		
		24	1000		
Oishiyama, Japan		1.5	150	active	Aki and Chouet (1975)
		3	200		
		6	300		
		12	450		
Garm, Tajikistan, central Asia	360;0.5			active	Rautian et al. (1978)
	60; 0.5				
Utah	325; 0.0025			active	Herrmann (1980)

Central California		10	600	active	Herrmann (1980)
Kanto, Japan		2	2000	active	Dainty (1981)
Friuli, Italy	80; 1.1			active	Rovelli (1982)
Hindu Kush, Afghanistan	360; 0.5			stable	Roecker et al. (1982)
Aeolian Islands, Southern Italy	181; 0.46	2	260	active	Del Pezzo et al. (1983)
		4	283		
		8	471		
Central United States	1000; 0.2			stable	Singh and Herrmann (1983)
Western United States	150; 0.45			active	Singh and Herrmann (1983)
Alaska		1.03-1.5	160-290	active	Biswas and Aki (1984)
New England	460; 0.4	0.75	105	active	Pulli (1984)
		1.5	204		
		3	395		
		6	765		
		8	1007		
		10	1264		
Northern Baja, California	37 ±13; 0.87±0.04			active	Robollar et al. (1985)
Kuril-Kamchatka		0.39	298	active	Gusev and Lemzikov (1985)
		0.71	367		
		1.51	227		
		2.96	307		
		5.5	414		
		11	722		
		24	1445		
Adak, Aleutian Islands	214;1.05	1.5	293	active	Scherbaum and Kisslinger (1985)
		3	1476		
		6	1074		
		12	4252		
California		3	250	active	Lee et al. (1986)
		12	1400		

Tangshan, China		1.97	186	active	Jin and Aki (1986)
Haichen, China		6.1	402	active	Jin and Aki (1986)
Northwest Pacific		1.5	442		Novelo-Casanova and Butler (1986)
		3	504		
		6	1267		
		12	2864		
		20	4447		
Central California-Sierra Nevada		1.5	100	active	Phillips et al (1988)
		24	525		
		24	2100		
		24	900		
Southern Mexico	441±16; 0.1 (*Lg* coda *Q*)			active	Canas (1988)
South Africa		2	496±166	stable	Shapira (1989)
Eastern Canada	657; 0.43			stable	Woodgold (1990)
British Columbia, Canada	110; 0.72	2	280	active	Zelt et al. (1999)
		16	850		
West Siberian Basin, Russia	380; 0.3			stable	Morozov et al. (2000)
Baja California Sur, Mexico	4.3 ± 0.6; 1.33±0.05			highly conductive body below	Wong et al., (2001)
	50 (±3); 0.65±0.20			stable area	
Southern Indian peninsular shield	730.62±0.09; 0.54±0.01			stable	Patanjali Kumar(2007)
	535.06±0.13; 0.59±0.01				
	150.56±0.08; 0.91±0.01				
South Korea	95 (±3.8); 0.94 (±0.02)	1.5	150	active	Yun et al. (2007)
		3	400		
		6,	700		
		9	850		

		12	1200		
		15	1500		
		18	1700		
Northern Italy		0.3-.05	217		
		0.5-0.7	227		
		0.7-1.0	270		
		1.0-1.5	262		
		1.5-2.0	313		
		2.0-3.0	386	active	Morasca el al. (2008)
		3.0-4.0	431		
		4.0-6.0	516		
		6.0-8.0	664		
		8.0-10.0	924		
		10.0-15.0	1143		
Southwest Anatolia	102; 0.82			active	Şahin S.(2008)